

## SMA/PDBI MULTIPLE LINE OBSERVATIONS OF THE NEARBY SEYFERT 2 GALAXY NGC 1068: SHOCK RELATED GAS KINEMATICS AND HEATING IN THE CENTRAL 100 PC?\*

M. KRIPS<sup>1</sup>, S. MARTÍN<sup>2</sup>, A. ECKART<sup>3</sup>, R. NERI<sup>1</sup>, S. GARCÍA-BURILLO<sup>4</sup>, S. MATSUSHITA<sup>5,6</sup>, A. PECK<sup>7,6</sup>, I. STOKLASOVÁ<sup>8</sup>, G. PETITPAS<sup>9</sup>, A. USERO<sup>4</sup>, F. COMBES<sup>10</sup>, E. SCHINNERER<sup>11</sup>, L. HUMPHREYS<sup>12</sup>, A.J. BAKER<sup>13</sup>

*Draft version November 13, 2018*

### ABSTRACT

We present high angular resolution ( $0''.5 - 2''.0$ ) observations of the mm continuum and the  $^{12}\text{CO}(J=3-2)$ ,  $^{13}\text{CO}(J=3-2)$ ,  $^{13}\text{CO}(J=2-1)$ ,  $\text{C}^{18}\text{O}(J=2-1)$ ,  $\text{HCN}(J=3-2)$ ,  $\text{HCO}^+(J=4-3)$  and  $\text{HCO}^+(J=3-2)$  line emission in the circumnuclear disk ( $r \lesssim 100$  pc) of the proto-typical Seyfert type-2 galaxy NGC 1068, carried out with the Submillimeter Array. We further include in our analysis new  $^{13}\text{CO}(J=1-0)$  and improved  $^{12}\text{CO}(J=2-1)$  observations of NGC 1068 at high angular resolution ( $1''.0 - 2''.0$ ) and sensitivity, conducted with the IRAM Plateau de Bure Interferometer. Based on the complex dynamics of the molecular gas emission indicating non-circular motions in the central  $\sim 100$  pc, we propose a scenario in which part of the molecular gas in the circumnuclear disk of NGC 1068 is radially blown outwards as a result of shocks. This shock scenario is further supported by quite warm ( $T_{\text{kin}} \geq 200$  K) and dense ( $n(\text{H}_2) \simeq 10^4 \text{ cm}^{-3}$ ) gas constrained from the observed molecular line ratios. The HCN abundance in the circumnuclear disk is found to be  $[\text{HCN}]/[^{12}\text{CO}] \approx 10^{-3.5}$ . This is slightly higher than the abundances derived for galactic and extragalactic starforming/starbursting regions. This results lends further support to X-ray enhanced HCN formation in the circumnuclear disk of NGC 1068, as suggested by earlier studies. The  $\text{HCO}^+$  abundance ( $[\text{HCO}^+]/[^{12}\text{CO}] \approx 10^{-5}$ ) appears to be somewhat lower than that of galactic and extragalactic starforming/starbursting regions. When trying to fit the cm to mm continuum emission by different thermal and non-thermal processes, it appears that electron-scattered synchrotron emission yields the best results while thermal free-free emission seems to over-predict the mm continuum emission.

*Subject headings:* Galaxies: individual: NGC 1068 – Galaxies: ISM – Galaxies: active – Galaxies: kinematics and dynamics – Galaxies: nuclei – Galaxies: Seyfert – Radio continuum: galaxies – Radio lines: galaxies – Submillimeter: galaxies

### 1. INTRODUCTION

Little is known about the effects of active processes in galaxies on the chemical and kinematic properties of

\* Based on observations carried out with the IRAM Plateau de Bure Interferometer. IRAM is supported by INSU/CNRS (France), MPG (Germany) and IGN (Spain).

<sup>1</sup> Institut de Radio Astronomie Millimétrique, Saint Martin d'Hères, F-38406, France; email: [krips,neri]@iram.fr

<sup>2</sup> European Southern Observatory, Alonso de Córdova 3107, Vitacura, Casilla 19001, Santiago 19 Chile; e-mail: smartin@eso.org

<sup>3</sup> Universität zu Köln, I.Physikalisches Institut, Zùlpicher Str. 77, 50937 Köln, Germany; email: eckart@ph1.uni-koeln.de

<sup>4</sup> Observatorio Astronómico Nacional (OAN) - Observatorio de Madrid, C/ Alfonso XII 3, 28014 Madrid, Spain; email: [s.gburillo,a.usero]@oan.es

<sup>5</sup> Institute of Astronomy and Astrophysics, Academia Sinica, PO Box 23-141, Taipei 10617, Taiwan, R.O.C.; email: satoki@asiaa.sinica.edu.tw

<sup>6</sup> Joint ALMA Observatory, Alonso de Córdova 3107, Santiago, Chile; email: apeck@alma.cl

<sup>7</sup> NRAO, 520 Edgemont Rd, Charlottesville, VA 22903

<sup>8</sup> Astronomical Institute of the Academy of Sciences of the Czech Republic, v.v.i., Boční II 1401, 14131 Prague, Czech Republic

<sup>9</sup> Harvard-Smithsonian Center for Astrophysics, SMA project, 60 Garden Street MS 78, Cambridge, MA 02138; email: gpetitpa@cfa.harvard.edu

<sup>10</sup> Observatoire de Paris, LERMA, 61 Av. de l'Observatoire, 75014 Paris, France; email: francoise.combes@obspm.fr

<sup>11</sup> Max-Planck-Institut für Astronomie, Königstuhl 17, 69117 Heidelberg, Germany; email: schinnerer@mpia.de

<sup>12</sup> ESO, Karl-Schwarzschild-Str. 2, D-85748 Garching, Germany; email: ehumphre@eso.org

<sup>13</sup> Department of Physics and Astronomy, Rutgers, the State University of New Jersey, 136 Frelinghuysen Road, Piscataway, NJ 08854-8019, USA; email: ajbaker@physics.rutgers.edu

the surrounding molecular gas and vice versa, whether the activity is in form of an active galactic nucleus (AGN) or a starburst (SB) or both. Information on the characteristics of the molecular gas in the vicinity of the activity is essential to reveal the underlying physical processes because molecular gas constitutes a large fraction of the fuel for the central activity and thus helps to keep it alive over cosmologically relevant time scales. Also, the feedback of activity onto the surrounding molecular gas represents an important factor for the evolution of the activity (with respect to outflows or shocks for instance). The large diversity and oftentimes also simultaneity of the physical processes accompanying the different activity types certainly complicate any interpretation of the interaction between the activity and the molecular gas. These processes include large scale shocks, gas out- and inflow, other dynamical perturbations, and strong radiation fields, such as through UV- or X-ray radiation, cosmic rays, or supernovae explosions (e.g., Martín et al. 2011; García-Burillo et al. 2010; Sakamoto et al. 2010; Papadopoulos 2010; Pérez-Beaupuits et al. 2009; Krips et al. 2008; Aalto 2008; Matsushita et al. 2007; García-Burillo et al. 2007; Martín et al. 2006; Usero et al. 2006; Sakamoto et al. 2006; Matsushita et al. 2005; Fuente et al. 2005; Meier & Turner 2005; Usero et al. 2004). Thus, a thorough study of the kinematics, excitation conditions and chemistry of the molecular gas close to AGN and SBs is essential for understanding the nature and evolution of these active environments.

High angular resolution observations of the  $^{12}\text{CO}$  emission, a reliable tracer of the global molecular gas reservoir, are an important step to study the dynamics in active galaxies.  $^{12}\text{CO}$  alone, however, can certainly not describe the complexity of the molecular gas close to the activity processes (especially with respect to the chemistry and excitation conditions of the molecular gas). Moreover,  $^{12}\text{CO}$  has been found to be an unreliable tracer of dense molecular gas environments (at least its lower rotational transitions), in which most AGN or star formation activity is supposed to take place (e.g., Krips et al. 2007; Gao & Solomon 2004). Observations at high angular resolution of different molecular tracers is thus a next logical step. Given recent upgrades of current (sub)mm interferometers, the detection and spatial resolution of weaker molecular lines becomes a feasible task.

In this paper we present high angular resolution observations of the (sub-)mm-continuum and  $^{12}\text{CO}$ ,  $^{13}\text{CO}$ ,  $\text{C}^{18}\text{O}$ ,  $\text{HCN}$  and  $\text{HCO}^+$  line emission in the nearby Seyfert type-2 galaxy NGC 1068, conducted with the Submillimeter Array (SMA) and the IRAM Plateau de Bure Interferometer (PdBI).

## 2. NGC 1068

The nearby Seyfert type-2 galaxy NGC 1068 (see Table 1 for a general overview) has become not only the figurehead for the viewing angle unification theory for Seyfert galaxies (e.g. Krolik & Kallman 1987), as its centre most impressively exhibits the characteristics for harboring an obscured type-1 Seyfert AGN (Antonucci & Miller 1985). It also advanced to a figurehead for the significantly different effects that AGN can have on the excitation conditions and chemistry of the surrounding molecular gas when compared to SB or quiescent galaxies (e.g. Krips et al. 2008; Usero et al. 2004; Kohno et al. 2001; Sternberg et al. 1994). The prototypical nature of NGC 1068 is certainly in part due to its relatively small distance (12.6 Mpc) from us and strong continuum as well as line emission from X-ray to radio frequencies, making it hence an ideal target to study the accretion and feedback processes of its active nucleus at unprecedented detail. As a (fortunate) consequence, a wealth of information is already available for this source, the most relevant of which will be summarised in this section.

The molecular gas in NGC 1068 is distributed in a starburst ring/spiral of  $\sim 3$  kpc ( $\sim 50''$ ) in diameter, a stellar bar of  $\sim 2$  kpc ( $\sim 30''$ ) in length and a circumnuclear disk/ring (CND) of  $\sim 200$  pc ( $\sim 3''$ ) in diameter (e.g., Schinnerer et al. 2000, and references therein). At the very center of the CND, pronounced  $\text{H}_2\text{O}$  maser emission suggests a thin disk of a few parsec in diameter (e.g., Gallimore et al. 2001; Greemhill et al. 1996). A pronounced jet and counter-jet can be observed from cm to mm wavelengths (e.g., Krips et al. 2006; Gallimore et al. 2004) that extends from the maser disk out to several kpc from the center. MIR observations reveal hot and ionised gas that biconically follow the path of the radio jet (e.g., Müller-Sánchez et al. 2009; Poncelet et al. 2008; Tomono et al. 2006; Galliano et al. 2004; Bock et al. 2000) and indicate the existence of a pc-scale warm dust torus (Jaffe et al. 2004). Early high-angular resolution radio-continuum observations indicated an interaction of the radio-jet with the neighbour-

ing interstellar medium (ISM) due to the apparently disrupted structure of the (northern) jet (radio components NE & C in, e.g., Gallimore et al. 1996; Roy et al. 1998). However, in a later publication, Gallimore et al. (2004) argue that the observed disturbed jet-structure (in NE) can as well be explained by variable outflow speeds due to variable accretion (e.g., Gallimore et al. 2001; Siemiginowska & Elvis 1997) though an earlier collision at position C was not discarded.

The complex dynamics of the molecular gas as traced by the  $^{12}\text{CO}(2-1)$  line emission within the CND were interpreted as a consequence of a warped disk (Schinnerer et al. 2000). However, more recent observations of the MIR rovibrational  $\text{H}_2$  emission start to raise doubts about this interpretation (e.g., Müller-Sánchez et al. 2009) and alternatively suggest that the complex gas kinematics are due to a funneling of the gas toward the AGN along the jet (inner 60 pc) plus an expanding ring (on scales of  $r=100-150$  pc), the latter having been already proposed a few years before by Galliano & Alloin (2002).

Additional fascinating characteristics of the CND of NGC 1068, besides the complex kinematic behaviour of its molecular gas, are its chemistry and excitation conditions which appear to significantly differ from starburst/star-forming environments. Traced by the “abnormal” line ratios of different molecules and transitions, mostly by  $\text{HCN}$ ,  $\text{HCO}^+$  and  $^{12}\text{CO}$ , it has been suggested that the CND in NGC 1068 harbors a giant X-ray-dominated-region (XDR; e.g., Kohno et al. 2008; Usero et al. 2004; Tacconi et al. 1994; Sternberg et al. 1994). XDRs are defined in a similar way to the Photon-Dominated-Regions (PDRs) in starburst galaxies (such as M82; e.g., Fuente et al. 2005) but are driven by X-ray rather than UV-radiation. High  $\text{HCN-to-CO}(J=1-0)$  ( $\geq 1$ ) and  $\text{HCN-to-HCO}^+(J=1-0)$  ( $\geq 1$ ) ratios are found in the CND of NGC 1068, indicating enhanced HCN abundances there. The X-ray radiation of the AGN is thereby supposed to be the main driver for the enhancement of HCN. It can penetrate much deeper into the surrounding molecular gas than the UV-radiation in PDRs leading to a stimulated “hyper”-production of HCN. A multi-transition, multi-molecular line study of HCN and  $\text{HCO}^+$  conducted with the IRAM 30m-telescope (Krips et al. 2008) supports an increased abundance of HCN and/or increased kinetic temperatures. Both can equally explain the elevated  $\text{HCN-to-}^{12}\text{CO}(1-0)$  line ratios either by the aforementioned enhancement of the HCN abundance and/or a hypo-excitation of the low- $J$   $^{12}\text{CO}$  transitions (see also M51 and NGC 6951 as examples of increased  $\text{HCN}/^{12}\text{CO}(J=1-0)$  ratios; Krips et al. 2009, 2007; Matsushita et al. 2007, 2004; Kohno et al. 1996).

Recent SiO interferometric observations of the CND in NGC 1068 carried out by García-Burillo et al. (2010) testify further to the complexity of the gas chemistry in this galaxy. The bright SiO emission in its CND suggests an enhanced abundance of this molecule which is interpreted by the authors as closely related to (high-velocity) shocks. The shocks are believed to be a consequence of a jet-gas interaction.

## 3. OBSERVATIONS

A summary of all (sub-)millimeter interferometric observations is given in Table 2, where observing parameters as well as achieved rms noise and angular resolutions are listed.

### 3.1. SMA

For all SMA observations, unless otherwise stated, the phase reference centre has been set to  $\alpha_{J2000} = 02^{\text{h}}42^{\text{m}}40.70^{\text{s}}$  and  $\delta_{J2000} = -00^{\circ}00'47''.9$  which corresponds to the radio position of the active nucleus (e.g. Gallimore et al. 2004; Krips et al. 2006). The SMA receivers have been tuned to the respective line using doppler-tracking on the systemic velocity of NGC 1068 of  $v_{\text{LSR}} = 1137 \text{ km s}^{-1}$ . Both the upper sideband (USB) and lower sideband (LSB) were used for the observations, yielding a bandwidth of 2 GHz each separated by 10 GHz. A spectral resolution of 0.81 MHz was used for all observations, corresponding to  $0.8 \text{ km s}^{-1}$  at 1 mm. The 225 GHz zenith opacity  $\tau_{225}$  was measured regularly throughout all observations at the nearby Caltech Submillimeter Observatory (CSO). The accuracy of the flux calibration for all tracks is estimated to be at a conservative level of  $\sim 20\%$ .

The SMA data have been reduced with SMA specific tasks in the MIR package (Scoville et al. 1993). Further image analysis has been conducted with the GILDAS package (Guilloteau & Lucas 2000).

#### 3.1.1. HCN( $J=3-2$ ) emission

We observed the HCN( $J=3-2$ ) line emission in NGC 1068 using the extended and very extended configurations with up to eight 6 m dishes in January, October and November 2006. The 345 GHz receivers were tuned to the HCN( $J=3-2$ ) line (265.886 GHz at rest) in the LSB; the USB was used for continuum measurements. The weather conditions were good with opacities of  $\tau_{225} = 0.05-0.1$  in the January track (extended configuration) and  $\tau_{225} = 0.13-0.22$  in the October/November tracks (very extended configuration). We used 3C273, 3C111 and/or 3C454.3 as bandpass and Uranus, Titan, and/or Neptune as flux calibrators<sup>14</sup>. We observed two quasars (0235+164, 0238-084, 0339-017, and/or 0423-013) every  $\sim 15$  minutes to calibrate the gains (amplitude and phase versus time). The data from all three tracks have been combined into one single data file, resulting in an rms noise of 24 mJy in  $17 \text{ km s}^{-1}$  wide velocity channels. The synthesized beam is determined to be  $1''.0 \times 0''.8$  at a position angle of  $\text{PA} = 30^{\circ}$  (natural weighting) and  $0''.53 \times 0''.46$  at  $\text{PA} = 30^{\circ}$  (robust weighting).

#### 3.1.2. HCO<sup>+</sup>( $J=3-2$ ) emission

We carried out observations of the HCO<sup>+</sup>( $J=3-2$ ) emission in NGC 1068 using seven antennas in extended configuration during November 2006. The 345 GHz receivers were tuned to the HCO<sup>+</sup>( $3-2$ ) line (267.558 GHz at rest) in the LSB; the USB was used for continuum measurements. The weather conditions were good with opacities of  $\tau_{225} = 0.06-0.15$ . Bandpass calibration was performed on 3C273, Titan and Uranus, while absolute fluxes were determined using Titan. The gains have been

<sup>14</sup> We used the line-free USB respectively for Titan and Neptune to determine the absolute flux level as they are known to have broad HCN lines which could contaminate a flux calibration in the LSB.

calibrated on 0423-013 and 0339-017. For this data set, we reach an rms noise of 33 mJy in  $17 \text{ km s}^{-1}$  wide velocity channels. The synthesized beam is determined to be  $1''.0 \times 0''.8$  at  $\text{PA} = 30^{\circ}$  (natural weighting).

#### 3.1.3. <sup>12</sup>CO( $J=3-2$ ) and HCO<sup>+</sup>( $J=4-3$ ) emission

The <sup>12</sup>CO( $J=3-2$ ) emission of NGC 1068 was observed in extended configuration using all eight antennas during September 2007. HCO<sup>+</sup>( $J=4-3$ ) was additionally observed in a separate track in August 2007. The 345 GHz receivers were tuned to the <sup>12</sup>CO( $J=3-2$ ) line (345.796 GHz at rest) in the LSB such that the HCO<sup>+</sup>( $J=4-3$ ) (356.734 GHz at rest) still falls within the USB. The opacities ranged between  $\tau_{225} = 0.06-0.13$ . Bandpass calibration was performed on 3C454.3 and Uranus. Uranus was also used for flux calibration. Gains were determined using 0238+166 and 0423-013. An rms noise of 80 mJy is reached in  $7 \text{ km s}^{-1}$  wide velocity channels. The synthesized beam is determined to be  $1''.0 \times 0''.8$  at  $\text{PA} = 30^{\circ}$  for natural weighting when also using a uv-taper to better match the angular resolutions of the other SMA observations. The original (un-tapered) angular resolution amounts to  $0.6 \times 0.5$  at  $\text{PA} = 30^{\circ}$ .

#### 3.1.4. <sup>13</sup>CO( $J=2-1$ ) and C<sup>18</sup>O( $J=2-1$ ) emission

The <sup>13</sup>CO( $J=2-1$ ) emission in NGC 1068 has been observed in extended configuration using all eight antennas during January and February 2008. The 230 GHz receivers have been tuned to the <sup>13</sup>CO( $J=2-1$ ) line (220.399 GHz at rest) in the USB such that the C<sup>18</sup>O( $J=2-1$ ) (219.560 GHz at rest), the HC<sub>3</sub>N( $J=23-22$ ) (209.230 GHz at rest) and H3 $\alpha$  (210.502 GHz at rest) still fall within the LSB. However, only the <sup>13</sup>CO( $J=2-1$ ) and C<sup>18</sup>O( $J=2-1$ ) line emission was detected. The opacities ranged between  $\tau_{225} = 0.1-0.2$ . Bandpass calibration was performed on 0423-013, 3C111 and Titan, while gains were determined using 0339-017 and 0423-013. Titan was further used as a flux calibrator. An rms noise of 12 mJy was reached in  $17 \text{ km s}^{-1}$  wide velocity channels. The synthesized beam is determined to be  $1''.0 \times 0''.9$  at  $\text{PA} = 30^{\circ}$  for natural weighting when also using a uv-taper to better match the angular resolutions of the other SMA observations.

#### 3.1.5. <sup>13</sup>CO( $J=3-2$ ) emission

The <sup>13</sup>CO( $J=3-2$ ) emission in NGC 1068 was observed in compact configuration using seven antennas in October 2005. These observations were part of the observing campaign presented by Humphreys et al. (2005), which aimed to detect extragalactic H<sub>2</sub>O maser emission at (sub-)millimeter wavelengths. The 345 GHz receivers have been tuned to the H<sub>2</sub>O(10(2,9)-9(3,6)) maser line (321.226 GHz at rest) in the LSB such that the <sup>13</sup>CO( $J=3-2$ ) line (356.734 GHz at rest) was still located within the USB. The 225 GHz zenith opacity has remained stable around 0.05-0.06. Bandpass calibration has been performed on 3C454.3, 3C111 and Uranus. Uranus has been also used as a flux calibrator. The gains were determined using 0234+285 and verified against 0215+015 and 0420-014. An rms noise of 61 mJy is reached in  $7 \text{ km s}^{-1}$  wide velocity channels. The synthesized beam is determined to be  $2''.4 \times 2''.1$  at  $\text{PA} = 28^{\circ}$  (natural weighting).

### 3.2. IRAM PdBI

#### 3.2.1. $^{12}\text{CO}(2-1)$ and $^{13}\text{CO}(J=1-0)$ emission

Observations of the  $^{12}\text{CO}(2-1)$  emission in NGC 1068 were carried out with the IRAM PdBI in February 2003 using all six antennas in A configuration. Simultaneously, we observed the  $^{13}\text{CO}(J=1-0)$  using the 3 mm PdBI receivers. The bandpass was calibrated on NRAO150 and 0420-014 while phase and amplitude calibration were performed on 0235+164 and 0238-084. A total bandwidth of 580 MHz with a spectral resolution of 1.25 MHz was used. We reach an RMS of  $\sim 7$  mJy in  $7 \text{ km s}^{-1}$  wide channels (natural weighting) at 1 mm and of  $\sim 1.9$  mJy in  $14 \text{ km s}^{-1}$  wide channels (natural weighting) at 3 mm. Applying natural weighting in the mapping process, beam sizes are derived to be  $1''.0 \times 0''.6$  at PA= $36^\circ$  at 1 mm and  $2''.5 \times 1''.7$  at PA= $28^\circ$  at 3 mm. However, to better match the SMA observations, we mapped the  $^{12}\text{CO}(2-1)$  data with a uv-taper giving an effective angular resolution of  $1.0'' \times 0.8''$  at PA= $30^\circ$ . As the uv-coverages between the SMA and PdBI data (for the high angular resolution data) are very similar, the usage of a simple uv-taper already provides the necessary accuracy to match the restoring beam of the PdBI observations with that of the SMA.

## 4. RESULTS

### 4.1. Continuum emission: from $850 \mu\text{m}$ to 1.4 mm

The sub(mm) continuum emission at the wavelengths presented in this paper was derived from the line-free channels of the respective line observations (Table 2), averaging emission from USB and LSB where possible (for the SMA data; the PdBI data were obtained from single-sideband observations). The continuum emission has further been merged between data sets with very similar observed frequencies (i.e., within  $\sim 10$  GHz). Before averaging data from different sidebands and/or observations, it has been carefully verified that the absolute flux, position and structure of the emission in the individual data sets are consistent with each other within the calibration uncertainties of 20% (flux) and  $0.1''$  (position) in order to reduce systematic errors.

The continuum emission is clearly detected at all wavelengths at a  $\geq 5\sigma$  level. To obtain accurate fluxes, positions and sizes, elliptical Gaussians were fitted to the data in the uv-plane, except for the uniformly weighted map of the 1.0 mm continuum emission for which a circular Gaussian was fitted given its apparently unresolved nature. The results of these fits are listed in Table 3.

The continuum emission at 1.0 mm (NA), 1.3 mm and 1.4 mm appear to be consistent with each other in terms of their flux, position and structure (see Table 3 and Fig. 1; see also Krips et al. 2006). All show peak fluxes of around 15-19 mJy/beam and spatially integrated flux densities of 22-28 mJy, indicating extended emission. Their positions, although self-consistent, are slightly to the North ( $\sim 0.2''$ ) of the radio position of the AGN (component S1 from Gallimore et al. 2004, marked with a white cross in Fig. 1) and that of the uniformly weighted 1.0 mm continuum emission (Fig. 1b; white contours). The shift between the mm and cm data is larger than the positional uncertainty of  $0.1''$  and thus assumed to be real. NGC 1068 is known to have a pronounced radio (and mm-) jet in a North-East-to-South-West direction,

of which the North-Eastern part exhibits the stronger emission (e.g., Gallimore et al. 2004; Krips et al. 2006). Despite the steep spectral index of the synchrotron emission of the jet, the extended (i.e.,  $>1''$ ) emission from both the jet and counter-jet are still visible at 3 mm (e.g., Krips et al. 2006; Schinnerer et al. 2000) but are significantly fainter or undetected at shorter wavelengths (i.e.,  $\lesssim 1$  mm).

The continuum emission at 1.0 mm (NA), 1.3 mm and 1.4 mm is a blend of emission associated with the (North-East) radio jet and the AGN itself (S1 in Gallimore et al. 2004) due to the 'lower' angular resolution of  $\sim 1''$ . Due to the higher angular resolution, the 1.0 mm continuum emission of the jet in the uniformly weighted map (Fig. 1b) is almost entirely resolved out leaving behind only the more compact emission of the AGN. Thus, the centroid of the emission at 1.0 mm (NA), 1.3 mm and 1.4 mm will naturally be shifted towards the North, while the 1.0 mm (UN) continuum emission should reveal the actual position of the AGN (or at least the base of the jet).

Going to even shorter wavelengths of  $850 \mu\text{m}$ , it appears that not only the continuum flux increases again, but also its position seems to be now consistent with the AGN, independent of the weighting (i.e., synthesized beam) used for mapping/cleaning and unlike the 1.0 mm (NA), 1.3mm, and 1.4 mm continuum emission. The latter may indicate that the emission from the radio jet is negligible at  $850 \mu\text{m}$  (see also Fig. 3 in Krips et al. 2006) and the AGN (i.e., the S1 component) dominates. The increased flux at  $850 \mu\text{m}$ , which appears to be larger by almost a factor of 2 compared to the 1.0 mm-1.4 mm emission, shows that thermal dust emission already plays a significant role at  $850 \mu\text{m}$  (see Section 5.1). Also, the size and shape of the continuum emission appear to have changed compared to that at longer wavelengths. The PA of the  $850 \mu\text{m}$  emission of  $\sim 90^\circ$  is significantly different from that ( $\sim 30^\circ$ ) of the 1.0 mm-1.4 mm emission. Moreover, the  $850 \mu\text{m}$  emission appears to be extended (Fig. 1c), in contrast to the 1.0 mm-1.4 mm emission, which seems to be extended only in the jet component but not in the 'left-over' AGN component in the uniformly weighted 1.0 mm map (Fig. 1b). The uniformly weighted  $850 \mu\text{m}$  continuum emission appears to be also resolved (white contours in Fig. 1c, compare also peak flux with total flux density in Table 3).

### 4.2. Line emission

#### 4.2.1. General Characteristics and Distribution of the Molecular Gas

The continuum emission has been subtracted from all line data in the uv plane to avoid any contamination of the line by continuum emission even if in some cases the continuum emission does not exceed the noise level in the individual channel maps (see Table 2 & 3). In order to reduce systematic effects due to spatial filtering, we used a slight uv-taper (giving some more weight to the shorter baselines) to map and clean all line emission data with the same synthesized beam, except for the high angular resolution ( $\sim 0.4-0.5''$ ) of the uniformly weighted HCN( $J=3-2$ ) map (shown additionally in Fig. 2a using white contours) and the low angular resolution ( $\sim 2''$ ) of the  $^{12}\text{CO}(J=1-0)$ ,  $^{13}\text{CO}(J=1-0)$  and  $^{13}\text{CO}(J=3-2)$  maps.

Fig. 2 shows the velocity integrated intensity maps of the molecular line emission from HCN(J=3-2), HCO<sup>+</sup>(J=3-2), HCO<sup>+</sup>(J=4-3), <sup>12</sup>CO(J=2-1), <sup>13</sup>CO(J=2-1), <sup>13</sup>CO(J=3-2), C<sup>18</sup>O(J=2-1), <sup>12</sup>CO(J=1-0) and <sup>13</sup>CO(J=1-0); <sup>12</sup>CO(J=3-2) is plotted in grey scale in all images to facilitate a comparison. All these molecules have been clearly detected above the 5 $\sigma$  level (except <sup>13</sup>CO(J=1-0)). The emission in all lines reveals a pronounced peak on the stronger eastern knot and in the stronger lines also a weaker peak on the western knot, both of which are already known from previous <sup>12</sup>CO observations (e.g., Schinnerer et al. 2000). An elliptical Gaussian has been fitted to the uv-data for all lines in order to obtain the position, peak- and spatially integrated flux of the emission in the two knots. The results of the fits are given in Table 4. The position of the emission in the eastern and western knot is very similar in all observed lines, excluding the <sup>13</sup>CO(J=2-1) and C<sup>18</sup>O(J=2-1) emission which seem to peak closer to the AGN.

The spectrum of the spatially integrated emission (over the central  $\sim 4''$ ) of each line is plotted in Fig. 3. We also show the <sup>12</sup>CO(J=1-0) line emission taken from Schinnerer et al. (2000) for consistency. While the velocity integrated line emission seems to be very similar in its shape and position for most lines, the line profiles vary significantly from each other. While for the dense gas tracers (HCN, HCO<sup>+</sup>) a single Gaussian fit is sufficient to reproduce the line profiles, the CO lines need a dual, triple or quadrupole Gaussian fit. However, to simplify a comparison, the results given in Table 5 represent a single Gaussian fit to all lines. The line centers are roughly consistent with each other, differing by less than 20 km s<sup>-1</sup>. Excluding the <sup>13</sup>CO(J=2-1) and C<sup>18</sup>O(J=2-1) emission, the line widths also agree with each other within the uncertainties. Except for the <sup>12</sup>CO(J=2-1) and <sup>13</sup>CO(J=2-1) line emission for which roughly half of the emission seems to be resolved out, the interferometric observations have captured most of the emission measured with single dish observations (Table 5). Please note that for the <sup>12</sup>CO(J=1-0) (Schinnerer et al. 2000) and <sup>13</sup>CO(J=1-0) emission, the single dish fluxes are much higher than the interferometric ones because they contain significant emission from the star-forming ring/spiral-arms and the bar.

#### 4.2.2. Dynamical Characteristics of the Molecular Gas

The kinematic behaviour of the different molecules is presented in detail in Fig. 4 to 11. To better understand the puzzling complexity of the different profiles of the various molecular lines and test whether it is due to dynamical effects, we spatially split the spectra by deriving the spectrum of the western and eastern knot separately (Fig. 4). Please note that the <sup>13</sup>CO(J=1-0) and C<sup>18</sup>O(J=2-1) line emission were discarded because of their insufficient sensitivity and/or lack of emission in the western knot while <sup>12</sup>CO(J=1-0) and <sup>13</sup>CO(J=3-2) are not included because of their insufficient angular resolution. The iso-velocity maps (Fig. 5) of the <sup>12</sup>CO, <sup>13</sup>CO, HCN and HCO<sup>+</sup> line emission clearly show a dynamical structure that seems to be dominated by standard disk rotation with a blueshifted eastern knot and a redshifted western knot. If disk rotation were the only underlying kinematics, one would expect to find a simple blueshifted

peak at the eastern knot and a redshifted peak at the western knot. Although disk rotation is observed, Fig. 4 shows kinematic features significantly differing from simple rotation. Instead, the blueshifted eastern knot also exhibits redshifted emission and the redshifted western knot blueshifted emission. These 'wings' appear to be present in all three <sup>12</sup>CO emission at a high significance level as well as in the <sup>13</sup>CO, HCN and HCO<sup>+</sup> emission but, given the lower signal-to-noise ratio (SNR) for these lines, not as pronounced as for <sup>12</sup>CO. At this point, it should be emphasized that in such a case the moment one map can be very misleading as it derives only the dominant kinematic structure and might overlook more complex underlying kinematics. Integrating (in velocity) the red- and blue-shifted parts of the line spectrum (Fig. 6) as well as analysing the channel maps (Fig. 7 & 8) might be the more appropriate approach. Fig. 6 indicates a more complex distribution than expected from simple disk rotation. We find blueshifted emission spatially coincident with redshifted emission and vice versa; this seems to be most pronounced for the <sup>12</sup>CO, <sup>13</sup>CO and HCN emission. By looking at the channel maps of the <sup>12</sup>CO(J=2-1) and <sup>12</sup>CO(J=3-2) emission (which have the highest SNR), the red- on blueshifted and blue- on redshifted emission is not only at low-velocities but also at higher velocities (which is especially visible in the <sup>12</sup>CO(J=2-1) emission; see channels  $< -70$  km/s and  $> +100$  km/s in Fig. 7). The same is true for the <sup>12</sup>CO(J=3-2) emission (Fig. 8, although less pronounced, especially for velocities  $> 80$  km s<sup>-1</sup> for which no emission can be found anymore as opposed to <sup>12</sup>CO(J=2-1)). We find a behaviour of the HCN(J=3-2) emission similar to that of the <sup>12</sup>CO(J=2-1) and <sup>12</sup>CO(J=3-2) emission though on a much lower significance level. The <sup>13</sup>CO(J=2-1) emission seems to indicate, however, a different behaviour (see Fig. 9). Instead of being distributed in a 'ring'-like manner, the emission appears to be elongated more in a South-West to North-East direction (see especially channels maps between  $+50$  km s<sup>-1</sup> to  $-20$  km s<sup>-1</sup>). However, given the low sensitivity level, this structure has to be treated with caution and needs confirmation by either higher sensitivity observations or other molecular lines such as SiO. Indeed, the SiO emission seems to indicate a similar behaviour as discussed in separate papers (see García-Burillo et al. 2008, 2010).

The position-velocity diagrams of the <sup>12</sup>CO and HCN emission, taken at different Position Angles (PA) in steps of 30° across the CND, are shown in Fig. 10. The grey scale denotes the <sup>12</sup>CO(J=2-1) emission for better comparison. Overall, the kinematic structures in the different lines strongly resemble each other. Also, the overlap of the red- on blueshifted emission can be seen quite well in the position-velocity diagrams (see especially PA=60-120° in Fig. 10), strongly indicating pronounced non-circular motions in the CND of NGC 1068.

In order to quantify and parametrise the observed complex kinematics, we follow the approach used by Heckman et al. (1989) and Baum et al. (1992). We determine three kinematic parameters from the slits taken at the different position angles used in Fig. 10 for the <sup>12</sup>CO emission. These parameters are: 1.) the average line-of-sight velocity dispersion  $\sigma$ , determined as  $0.426 \times \text{FWHM}$  along each slit, 2.) the "rotational" velocities  $\Delta$ , determined from the difference between the aver-

age velocities on either side of the nucleus along each slit, and 3.) the rms variation of the velocity  $\epsilon$  for each point along the slit, defined as  $\epsilon = \sqrt{\frac{1}{N} \sum_{i=1}^N (v_i - v_{av})^2}$ , where  $N$  is the number of points along the slit,  $v_i$  the intensity weighted velocity for point  $i$  and the  $v_{av}$  the intensity weighted average velocity along the slit. A comparison of the different parameters with each others, especially the ratios  $\frac{\Delta}{\sigma}$  and  $\frac{\Delta}{\epsilon}$  allows to classify the dynamics into three different groups (for a more detailed explanation we refer to Baum et al. (1992)):

ROTATORS:  $\Delta/\sigma \gtrsim 1$ ,  $\Delta/\epsilon \gtrsim 1$

CALM NON-ROTATORS:  $\Delta/\sigma < 1$ ,  $\Delta/\epsilon \sim 1$

VIOLENT NON-ROTATORS:  $\Delta/\sigma < 1$ ,  $\Delta/\epsilon < 1$

The results of this kinematical parametrisation for the  $^{12}\text{CO}(J=2-1)$  are shown in Fig. 11, highlighting our previous findings (we find very similar values when taking the  $^{12}\text{CO}(J=3-2)$  emission). For most position angles, we find that the ratios are most consistent with calm non-rotation with one exception ( $\text{PA}=60^\circ$ ) being located in the area of the violent non-rotators. This strongly emphasizes the fact that although there is an underlying dominating disk rotation, the dynamics of the molecular gas in the CN of NGC 1068 is significantly disturbed by a non-rotational process, most significantly for the North, North-Eastern part of the CN (i.e., along  $\text{PA}=0-90^\circ$ ). We also attempted to determine the rotational velocities directly from azimuthally averaging the velocities within the CN and then subsequently fitting rotational curves to the data using `rotcurv` in `gipsy`. We thereby assumed different scenarios ranging from pure disk rotation to adding a radial dependency. However, no physically meaningful result could be obtained. We mostly find positive velocities that decrease with radius which is inconsistent with simple disk rotation (see also the dynamical analysis done in Schinnerer et al. 2000) and necessitates the inclusion of a bulge or central mass component whether in form of nuclear star cluster or a massive black hole in addition to the disk. This certainly further emphasizes the complexity of the molecular gas dynamics in the CN of NGC 1068.

#### 4.2.3. Molecular Line Ratios

In order to constrain the excitation conditions and chemistry of the molecular gas, we derive the line ratios for the different molecules and transitions in several ways, by accounting for the different angular resolutions (especially with respect to the  $^{12}\text{CO}(J=1-0)$ ,  $^{13}\text{CO}(J=1-0)$  and  $^{13}\text{CO}(J=3-2)$  emission). Before determining any line ratio, the line emission was brought to the same (lower) angular resolution by using a uv-taper; this seems appropriate for most of the lines as we recovered most of the emission with the interferometric observations. Also, we compute line ratios only for emission coming from the same spatial regions (see Figs.12-14). Fig. 12 shows the velocity integrated line ratios between various combinations of the molecular lines. Separating spatially the eastern and western knot we derive spatially averaged line ratios from Fig. 12 which are listed in Table 6. Please note that the values in Table 6 might vary from those derived from Tables 4 and 5. However, the

differences can be easily explained by the different sequence of averaging (i.e., first in space, then in velocity versus first in velocity, then in space) for Table 5, the usage of an elliptical Gaussian fit<sup>15</sup> for Table 4 as opposed to spatially averaging without a fit as done for Table 6, and the different spatial resolutions of the line emission in Tables 4 & 5.

We identify some spatial variance of the different line ratios (mostly a factor  $\sim 2-3$ ) which seem to be most pronounced in the  $^{12}\text{CO}$  and  $^{13}\text{CO}$  line ratios (Fig. 12a,d,o). The HCN and  $\text{HCO}^+$  line ratios seem to be more constant over the CN than  $^{12}\text{CO}$  and  $^{13}\text{CO}$ . The higher values are found closer to the position of the AGN for most maps.

In order to investigate whether there might be a velocity (and spatial) dependence on the line ratios, we determined the line ratio channel maps for the two strongest  $^{12}\text{CO}$  transitions ( $J=2-1$  and  $J=3-2$ ) as function of velocity in Fig. 13. We find somewhat higher (i.e., factor of  $\gtrsim 2$ )  $^{12}\text{CO}(J=3-2)$ -to- $^{12}\text{CO}(J=2-1)$  ratios close to the AGN at velocities around the systemic velocity but also on the eastern knot at high negative velocities ( $\lesssim -130 \text{ km s}^{-1}$ ). Both knots seem to show (more or less) the same velocity and spatial behaviour as can be seen in Fig. 14. This plot shows the spatially averaged  $^{12}\text{CO}(J=3-2)$ -to- $^{12}\text{CO}(J=2-1)$  line ratios for the eastern and western knot as function of velocity. The two curves follow each other nicely except for velocities between  $-120$  to  $-140 \text{ km s}^{-1}$  for which the eastern knot exposes higher values (by a factor of 2). The error bars denote the variance of each averaged value which in most cases indicates a variation by a factor of 1.5.

## 5. DISCUSSION

### 5.1. Spectral Energy Distribution of the Continuum Emission

The nature of the continuum emission (from IR over sub-mm to cm wavelengths) represents a highly debated and complicated matter for NGC 1068, recently gaining a revival by newly published VLTI/MIDI (i.e., IR) and radio data (e.g., Hönig et al. 2008; Cotton et al. 2008). As mentioned in the previous section, the radio continuum emission splits up into several components, a jet plus counter-jet and a core component (S1) associated with the AGN itself. While the emission from the jet is certainly pure non-thermal synchrotron emission, as supported by its steep continuum spectrum (e.g., Gallimore et al. 2004; Cotton et al. 2008), the nature of the emission from S1 is highly controversial. Gallimore et al. (2004) already rule out synchrotron emission as origin for the continuum spectrum of S1 and discuss electron-scattered synchrotron emission as well as thermal free-free absorption as alternatives. While Krips et al. (2006) present arguments for electron-scattered synchrotron emission based on a turnover seen between cm and mm-data, Cotton et al. (2008) rather support the thermal free-free absorption model. A highly complicating factor in this discussion is certainly the mismatch in angular resolution between the

<sup>15</sup> Although this a reasonable first order fit, the line emission is certainly not exactly of an elliptical Gaussian shape so that some of the emission is not well reproduced by fitting an elliptical Gaussian to the velocity integrated maps.

cm, mm and IR data. As discussed in Krips et al. (2006) and this paper, the mm-continuum emission is contaminated by emission from the jet at angular resolutions of  $\gtrsim 1''$ , introducing large uncertainties in the estimate of S1's flux (compare Hönic et al. 2008; Cotton et al. 2008; Krips et al. 2006) due to the lack of angular resolution. However, the previous estimate of the 1.3 mm continuum flux of  $(10 \pm 4)$  mJy in Krips et al. (2006), translating to  $(9 \pm 4)$  mJy at 1.0 mm, is very similar to the *measured* 1.0 mm continuum flux of  $(13 \pm 2)$  mJy from our high-angular resolution SMA observations. Given the unresolved nature of the latter, jet emission does not seem to be significant anymore at this angular resolution (see also Fig. 1 in Cotton et al. 2008) although the obtained angular resolution is still an order of magnitude larger than that at cm wavelengths.

Taking also the new 850  $\mu\text{m}$  (UN) continuum flux measurements into account, we recomputed the spectral energy distribution (SED) and replotted the models used by Hönic et al. (2008) and Krips et al. (2006). We thereby base our graphs on the formula and parameters specified in Equations (2)-(5) and Table 2&3 in Hönic et al. (2008) and Equations (1)-(2) and Fig. 3 in Krips et al. (2006). The results are shown in Fig. 15a-c. We marked all data points with a circle for which the obtained angular resolution of the observations did not exceed  $1''^{16}$ . We also fitted a two-temperature grey body to the IR data, in order to estimate the contribution of thermal dust emission to the sub-mm continuum emission. Although this grey-body fit is certainly not as sophisticated as the clumpy torus model used in Hönic et al. (2008), it represents a reasonable approximation as demonstrated by the good match to the IR data points.

As can be seen in Fig. 15b and c, the models used by Hönic et al. (2008) significantly overestimate the observed 1 mm (UN) flux by a factor of 2-3, although they reproduce correctly the 850  $\mu\text{m}$  one. It seems that the electron-scattered synchrotron emission model in Fig. 15a and the thermal free-free emission model in Fig. 15c both need the extra contribution from the thermal dust emission to correctly reproduce the 850  $\mu\text{m}$  (UN) flux, while the synchrotron model in Fig. 15b does not require it. Thus, it appears to be indeed very likely that the continuum emission is dominated by thermal dust emission starting at wavelengths  $\lesssim 850 \mu\text{m}$ , as posited above.

Based on the 1 mm (UN) flux, it seems that the model best reproducing the SED at cm and mm wavelengths is the electron-scattered synchrotron emission; the thermal free-free absorption seems to overpredict the 1 mm flux. However, observations of the continuum emission in NGC 1068 have to be conducted at similarly high angular resolutions ( $\ll 0.5''$ ), in order to dispel all remaining doubts, although the new mm observations presented in this paper are already a step in the right direction.

## 5.2. Dynamics of the Molecular Gas

In previous studies, the complex kinematic behaviour of the molecular gas has been thought to be a consequence of a warped disk. The warped disk has been

modelled with a tilted ring model (e.g., Schinnerer et al. 2000). However, the spatial overlap between the red- and blueshifted emission (i.e., the existence of highly non-circular motions) cannot be reproduced by these tilted ring models because they are based on circular motions and thus cannot account for non-circular motions of the gas (within the plane).

Even though we cannot rule out a warped disk scenario in which part of the gas could be trapped in elliptical orbits producing the non-circular motions, we want to propose an alternative approach, following recent findings on the  $\text{H}_2(1-0)$  S(1) emission at scales of 100-150 pc by Müller-Sánchez et al. (2009) and the model proposed by Galliano & Alloin (2002). The nature of the dynamics displayed in Fig. 4, 5, 6, 7 and 8 could also be explained by the following scenario: a rotating disk plus an outflow of the disk gas due to shocks and/or a CND-jet interaction. This hypothesis seems to further gain support when considering besides the  $\text{H}_2$  1-0 S(1) map (Müller-Sánchez et al. 2009, see their Fig. 4), also the 12  $\mu\text{m}$  map (Bock et al. 2000, see their Fig. 4) and the 5 cm radio-continuum map (Gallimore et al. 2004, see their Fig. 1). The  $\text{H}_2$  1-0 S(1) and 12  $\mu\text{m}$  emission follow nicely that of the radio jet in the inner  $1''$  (North/North-East direction) which seems to interact with emission from the molecular gas in the CND at  $\pm 1-2''$  in the Northern part (see next Sub-Section); both the blue and red-shifted components associated with the non-circular motions to the East and West of where the jet goes through or lies in front of the CND (see also the case of M51; Matsushita et al. 2007, 2004). As the jet shows a biconical structure with a change in direction close to the CND, it is not unreasonable to believe that part of it indeed hits the CND (see also Kraemer et al. 1998). Such an interaction could easily produce a shock through/along the CND (at least in the northern part, i.e. the bridge between the eastern and western knot) feeding the assumption that some part of the molecular gas in the ring/disk might be blown outwards.

Other causes for expanding/shocked gas include hypernovae explosions, stellar winds from a super stellar cluster as suspected in some nearby starburst galaxies (such as NGC 253 or M82, Sakamoto et al. 2006; Matsushita et al. 2000) or cloud-cloud collision within the CND (i.e., within the inner Lindblad resonance; see García-Burillo et al. 2010). However, they seem rather unlikely since the CND of NGC 1068 does not show any signs of starburst activity and the expansion seems to be too "ordered", i.e., too symmetric, to be caused by highly chaotic cloud-cloud collisions. Also, we cannot entirely rule out that the dynamics we see in the molecular gas is due to inflowing rather than outflowing gas, especially since indications of inflowing gas along the jet within the central  $\sim 70$  pc (i.e., on scales smaller than the CND) have been already presented in previous studies (see Müller-Sánchez et al. 2009). However, based on the appearance of the molecular gas within the disk (ring-like structure with an apparent void of gas in the inner part) lets us favor the jet-gas interaction rather than an inflow scenario (on scales of 100-150 pc). An outflow on scales of 100-150 pc is not necessarily in contradiction with an inflow scenario on scales  $\lesssim 70$  pc proposed by Müller-Sánchez et al. (2009). The jet-gas interaction could equally drag gas outwards on scales larger than

<sup>16</sup> Please note, that this is true for all data points except that at 3 mm. The encircled S1 data point has been estimated at 3 mm, not observed. We added this data point for consistency reasons only.

100 pc but trigger an inflow at smaller scales, depending on the type of interaction between the jet and the molecular clouds. However, higher-angular resolution observations at sub-arcsecond angular resolution (as possible with ALMA) will certainly help to distinguish between the different scenarios.

Based on this alternative approach, we tried to reproduce the molecular gas dynamics with a very simplistic model that includes a dominant (Keplerian) rotating disk plus an outflow of some of the disk gas. We thereby assume a velocity gradient of  $\Delta v_0 = 200 \text{ km s}^{-1}$ , a radius of  $\sim 1.2''$  and an inclination of  $\sim 60^\circ$  for the rotating disk. We additionally add a slight ellipticity of 5% and asymmetry ratio between the eastern and western part of 1:0.7 to the model. The outflow is approximated by a slightly expanding elliptical ring. We assume the same ellipticity of 5% as before and that the expansion starts at the inner radius of the disk. The expansion rate (H) is chosen to be  $200 \text{ km s}^{-1}$  per  $1''$  or  $67 \text{ pc}$  equivalently (i.e.,  $H = 3 \text{ km/s/pc}$ ); this value is similar to what has been estimated for M51 ( $2.2 \text{ km/s/pc}$ ; Matsushita et al. 2007). We also introduced a slight asymmetry ratio of 1:0.9 between the blue- and redshifted emission. We further assume that up to  $\sim 30\%$  of the disk gas is expanding. Most of these values that were chosen for the model parameters were almost instantly obvious from the observations, especially the velocities and radii. We hence used them as starting values and scanned then through a reasonable parameter space for the optimal combination of input values that matches best the observed maps. However, given the larger number of parameters used in this model and hence the many degrees of freedom, we did not actually conduct a true fit to the data but rather a “fit” by eye. The results of this so found “best-fit” model are displayed and compared to the  $^{12}\text{CO}(J=2-1)$  emission in Fig. 16-20. Indeed, the major dynamical characteristics of the molecular gas emission can be reproduced by this simplistic model supporting the hypothesis of an additional gas outflow. Also, using the same kinematic parametrisation for the model as used for the  $^{12}\text{CO}$  emission (see Fig. 11), we find very similar ratios between the observed and simulated emission. We have to stress that this suggestion does not exclude a warped CND but it is not needed for this model.

It is interesting to note as further support for our approach that the distribution of the  $\text{HCN}(J=3-2)$  emission matches almost exactly that of  $\text{H}_2 1-0 \text{ S}(1)$  in the CND, even better than the  $^{12}\text{CO}(J=2-1)$  emission (see Fig. 1 in Müller-Sánchez et al. 2009). Similar to the  $\text{H}_2$  map that indicates the brightest emission toward the North, also most of the  $\text{HCN}$  emission is found toward the northern part of the CND at which most of the potentially shocked gas would lie. Thus, one would expect the densest (and hottest) part of the gas in that area (see next section).

### 5.3. Excitation conditions of the gas

The line ratios derived from the interferometric maps, especially for the  $\text{HCN}$ ,  $\text{HCO}^+$  and  $^{12}\text{CO}$  emission (Fig. 12 and Table 6), are consistent with previous findings from single-dish observations (e.g., Krips et al. 2008). They support a picture in which the molecular gas in the CND is relatively dense ( $n(\text{H}_2) \leq 10^{4.5}$ ) and warm ( $T_k > 40 \text{ K}$ ) with potentially higher than normal (i.e., in galactic giant molecular clouds)

$\text{HCN}$  abundances ( $Z(\text{HCN}) = [\text{HCN}]/[\text{H}_2]$ ) of  $Z(\text{HCN}) = 1-50 \times Z_{\text{galactic}}(\text{HCN})$  ( $Z_{\text{galactic}}(\text{HCN}) = 2 \times 10^{-8}$ ; e.g., Irvine 1987). Krips et al. (2008) argue that the high  $\text{HCN}$ -to- $^{12}\text{CO}(J=1-0)$  and  $\text{HCN}$ -to- $^{13}\text{CO}(J=1-0)$  in NGC 1068 can be explained by either higher than normal  $\text{HCN}$  abundances due to an XDR (see also Usero et al. 2004; Sternberg et al. 1994) and/or higher gas temperatures leading to hypo-excited  $\text{CO}(J=1-0)$  emission. The latter is supported by decreasing  $\text{HCN}$ -to- $\text{CO}$  line ratios with increasing rotational number  $J$ . However, strong constraints on the kinetic temperatures could not be set based on the single-dish observations alone. Also, most single-dish observations are unable to unambiguously distinguish between the molecular gas emission in the center and that in the star-forming spiral arms, complicating any interpretation of the data. Furthermore, most of the interferometric data previously published mostly focus on  $^{12}\text{CO}$  at moderate angular resolution and only two of its transitions.

The new interferometric maps, obtained for several transitions and molecules at sufficiently high angular resolution, overcome some of the short-comings of previous observations/analyses.

In the following we will discuss results from simulations of the excitation conditions of the molecular gas carried out with the radiative transfer code RADEX developed by Van der Tak et al. (2007). Please note that we did not find significant difference when using the LVG code in MIRIAD or the RADEX code. Given simplified simulations with RADEX, we decided to use RADEX in this paper as opposed to Krips et al. (2008) in which an LVG code was used.

RADEX offers three different possibilities for the escape probability method: a) a uniform sphere, b) an expanding sphere (Large-Velocity-Gradient, LVG), and c) a plane parallel slab (shock). We used all three methods but did not find significant differences for our data between them. Thus, in order to keep the interpretation as simple as possible, we will discuss the results with respect to a uniform sphere in the following.

We carried out simulations with RADEX for each molecule using the following grid of parameters (dimension:  $51 \times 51 \times 51$ ):

- Kinetic Temperature:  $T_{\text{kin}} = 1 - 500 \text{ K}$
- Gas density:  $n(\text{H}_2) = 10^3 - 10^7 \text{ cm}^{-3}$
- Column density:  $N(^{12}\text{CO}) = 10^{13} - 10^{21} \text{ cm}^{-2}$

We define the abundance ratio between one molecule (MOL1) and another (MOL2) as  $X_{\text{MOL2}}^{\text{MOL1}} \equiv Z(\text{MOL1})/Z(\text{MOL2})$  with  $Z(\text{MOL1}) \equiv [\text{MOL1}]/[\text{H}_2]$ . For the different molecular abundance ratios we assume the following ranges:

- Abundance ratios:
 
$$X_{^{13}\text{CO}}^{^{12}\text{CO}} \simeq 6-1000$$

$$X_{\text{HCO}^+}^{\text{HCN}} \simeq 1-500$$

The ranges were chosen such that they span the abundance ratios found in different (galactic and extragalactic) environments. In the Milky Way typical values of the  $^{12}\text{C}/^{13}\text{C}$  abundance ratio are  $\sim 20$  which

increase to values of 80-100 in the outer parts of the galaxy (e.g. Wilson & Rood 1994; Wilson & Matteucci 1992). Nearby starburst galaxies and ULIRGs show somewhat higher  $^{12}\text{C}/^{13}\text{C}$  abundance ratios of  $>30$  than found in the Galactic Center (e.g., NGC 253, M82, IC 342, NGC 4945, NGC 6240 see Greve et al. 2009; Henkel et al. 1998, 1994, 1993a; Henkel & Mauersberger 1993b) with Arp 220 being the exception. Greve et al. (2009) find a very low abundance ratio of only 8 for this galaxy. Furthermore, some high redshift galaxies seem to exhibit also rather high  $^{12}\text{C}/^{13}\text{C}$  values of  $>30$  as determined for the ISM in the gravitational lens of PKS 1830–211 (Muller et al. 2006) or the Cloverleaf (Henkel et al. 2010). Values of  $X_{\text{HCO}^+}^{\text{HCN}}$  show an equally large scatter ranging from the order of unity in starforming regions in the Milky Way (such as Orion and SgrB2; see Blake et al. 1987) and nearby starburst galaxies/ULIRGs (such as M82, NGC 2146, NGC 253, NGC 4945, NGC 6240 and Arp 220; see Naylor et al. 2010; Greve et al. 2009; Krips et al. 2008; Wang et al. 2004) to  $\geq 10$  in nearby Seyfert galaxies (e.g., Krips et al. 2008).

For the simulations, we will concentrate on the region of the CNB that contains all molecules. This region corresponds to the bridge between the eastern and western knot, i.e., the northern part of the CNB, and has a size of roughly  $\sim 2\text{--}3''$  ( $\simeq 120\text{--}180$  pc). This corresponds to roughly up to 50% of the molecular gas in the CNB. If jet interaction indeed plays a role in NGC 1068, this will be the region most obviously affected.

### 5.3.1. $^{12}\text{CO}$ & $^{13}\text{CO}$ emission

We conducted a  $\chi^2$ -test on the RADEX grid by using the observed line ratios for the  $^{12}\text{CO}$  and  $^{13}\text{CO}$  line emission. Fig. 21 shows the parameters for the best  $\chi^2$ -test for four exemplary abundance ratios (10,26,52,110) from the aforementioned range; abundance ratios at the lower and higher end of the range show somewhat higher  $\chi^2$  values.

The middle panel shows the lowest  $\chi^2$  found in each range of column densities and abundance ratios. The lower and upper panels show the respective lower and upper limits for the column density for which still a reasonably low  $\chi^2$  was found to indicate the spread in column densities.

The availability of the three lowest transitions for  $^{12}\text{CO}$  and  $^{13}\text{CO}$  allows us to set tight constraints on  $T_{\text{kin}}$ ,  $n(\text{H}_2)$  and  $N(^{12}\text{CO})$ . The observed CO line ratios most impressively restrict the kinetic temperatures to values well above 200 K. This strengthens previous indications of warm/hot ( $T_{\text{kin}} > 50$  K) molecular gas in the CNB of NGC 1068 (Kamenetzky et al. 2011; Krips et al. 2008; Matsushita et al. 1998; Sternberg et al. 1994) but being much higher than the value found by Tacconi et al. (1994). However, Tacconi et al. (1994) base their simulations on single-dish data which cannot distinguish well between emission from the starforming ring/spiral arms and the CNB. Especially the  $^{13}\text{CO}(J=1-0)$  emission might be overestimated for the CNB which clearly is hardly detected in the interferometric map despite the high sensitivity of the observations. The lowest  $\chi^2$  is actually found for kinetic temperatures around 450 K, which seems to be fairly high. Although we used a one-gas component model due to the lack of sufficient

observational constraints (i.e., higher-J CO transitions with  $J_{\text{upper}} \geq 4$ ), we do not expect all of the gas to be at these high kinetic temperatures, but rather a fraction of the gas in the northern part of the bridge. It seems likely that by using a two-temperature model for the molecular gas, we may find slightly lower maximum temperatures. However, this necessitates either the inclusion of CO data at higher-J transitions or using so called molecular thermometers (such as  $\text{H}_2\text{CO}$  or  $\text{NH}_3$ ; see Ao et al. 2011). High kinetic temperatures would be expected in several scenarios, among them shocks as well as heating through X-ray radiation from the AGN (e.g., Meijering et al. 2007; Meijering & Spaans 2005). Nevertheless, a significant fraction ( $>> 10\text{--}20\%$ ) of the warm molecular gas in this bridge regions seems to exhibit high kinetic temperatures which is a much larger fraction than so far found (for the overall molecular gas reservoir) in starburst and other Seyfert galaxies ( $\leq 30\%$ , see for instance Roussel et al. 2007; Dale et al. 2005; Rigopoulou et al. 2002).

The density is also well constrained and is found to be in the range of  $10^{3.5}\text{--}10^{4.5} \text{ cm}^{-3}$ , consistent with previous findings (Krips et al. 2008; Matsushita et al. 1998). Considering the range of assumed abundance ratios, the column density of  $^{12}\text{CO}$  approximately spans a range between  $\sim 10^{17.0} \text{ cm}^{-2}$  and  $10^{19.0} \text{ cm}^{-2}$ . Even though CO might not be the best tracer of the  $^{12}\text{C}/^{13}\text{C}$  isotopic ratio (e.g., Martín et al. 2010) we assume it to be a first approximation to this ratio. The carbon ratio of 26 found for the absolute lowest  $\chi^2$  is similar to the value of 20 measured in the Galactic Center region (e.g., Wilson & Rood 1994) and lower than that derived towards nearby starbursts (e.g., Henkel et al. 1993a; Henkel & Mauersberger 1993b; Henkel et al. 1994). Such  $^{13}\text{C}$  enrichment would point towards a highly nuclear processing of the ISM in the central region of NGC 1068.

### 5.3.2. $\text{HCN}$ & $\text{HCO}^+$ emission

In Krips et al. (2008) we carried out an LVG analysis for NGC 1068 based on the HCN and  $\text{HCO}^+$  single-dish lines ratios with kinetic temperatures not exceeding 200 K. As our new simulations indicate kinetic temperatures lying significantly above 200 K, we repeated the simulations with RADEX allowing for a larger range in kinetic temperatures. The line fluxes for the HCN and  $\text{HCO}^+(J=1-0)$  emission are taken from PdBI observations at  $\sim 1''$  angular resolution (García-Burillo et al. 2008) which will be analysed in more detail in a later paper by Usero et al. (in prep.). The results of the RADEX simulations for HCN and  $\text{HCO}^+$  are shown in Fig. 22.

Considering the restrictions for the kinetic temperatures ( $> 200$  K), we find solutions (i.e., with low  $\chi^2$ ) with RADEX for which the HCN-to- $\text{HCO}^+$  abundance ratio lies between  $X_{\text{HCO}^+}^{\text{HCN}} \simeq 10\text{--}500$  which is higher than that found in starforming/starbursting regions ( $X_{\text{HCO}^+}^{\text{HCN,g}} \simeq 1$ ). However, good solutions are also found for lower kinetic temperatures. This is due to the fact that HCN and  $\text{HCO}^+$  are not as sensitive to changes in the kinetic temperatures as  $^{12}\text{CO}$  and  $^{13}\text{CO}$ . They are better indicators of changes in the volume density, as can be nicely seen in Fig. 22; the volume density is restricted by the  $\chi^2$ -test to a very small area and independently yields values of  $n(\text{H}_2) \simeq 10^{3.5}\text{--}10^{4.5} \text{ cm}^{-3}$  similar to the  $^{12}\text{CO}$  and  $^{13}\text{CO}$

results.

The simulations<sup>17</sup> indicate column densities for HCN in the range of  $N(\text{HCN}) \simeq 10^{12.0-10^{13.5}} \text{ cm}^{-2}$  which is smaller (a factor of  $\sim 10$ ) than what was found by Krips et al. (2008) with the LVG code. However, results are quite similar to Krips et al. (2008) when assuming similar kinetic temperatures.

Comparing the HCN column densities to those of  $^{12}\text{CO}$  ( $N(^{12}\text{CO}) \simeq 10^{17.0-10^{19.0}} \text{ cm}^{-2}$ ), we obtain abundance ratios between HCN and  $^{12}\text{CO}$  of  $X_{\text{HCN}}^{^{12}\text{CO}} \gtrsim 10^{3.5}$  which seems to be still compatible with a slightly increased abundance of HCN. Comparing the column densities of  $\text{HCO}^+$  and  $^{12}\text{CO}$ , we find a somewhat decreased  $\text{HCO}^+$  abundance (by a factor of at least 10 lower than found in galactic starforming regions). This agrees well with previous results (e.g., García-Burillo et al. 2010; Krips et al. 2008; Usero et al. 2004) suggesting an increased formation (and hence increased abundance) of HCN due to an XDR in the center of NGC 1068.

## 6. SUMMARY & CONCLUSIONS

The SMA and PdBI observations of the (sub)-mm emission in NGC 1068 presented in this paper show a complex distribution, kinematics and excitation conditions of the molecular gas. The (sub)mm continuum and molecular line emission is interpreted as follows:

- 1.) The cm/mm-continuum emission seems to be best reproduced by electron-scattered synchrotron emission. Thermal free-free emission as proposed by Hönlig et al. (2008) overpredicts the high angular resolution 1 mm continuum emission.
- 2.) The molecular gas is found to display a very complex kinematic behaviour in the  $^{12}\text{CO}$ , HCN and  $\text{HCO}^+$  lines which is not reproducible by a tilted-ring model approximating a warped disk with circular motions. Instead, a dominant rotating disk plus a radial outflow of some of the gas in the CND

is proposed as an alternative explanation to account for the non-circular motions.

- 3.) The different line ratios from the  $^{12}\text{CO}$ ,  $^{13}\text{CO}$ , HCN, and  $\text{HCO}^+$  emission seems to be consistent with moderately dense and warm gas, both being further support for a gas scenario in which heated and compressed by a shock (at least in the North/North-Eastern part of the ring). The highest line ratios are found close to the AGN and/or jet-CND 'contact'-point. In this picture, the increased kinetic temperatures seem to be one of the culprits for the unusually high HCN-to- $\text{CO}(J=1-0)$  line ratios due to a hypo-excitation of the  $\text{CO}(J=1-0)$  line emission.
- 5.) Consistent with previous papers, we find further indications of an increased HCN abundance in NGC 1068 (by a factor of  $\sim 4-10$ ), and a decreased  $\text{HCO}^+$  abundance (by a factor of  $\sim 5-10$ ), explaining the high HCN-to- $\text{HCO}^+$  abundance ratio in the CND of this source.

The Submillimeter Array is a joint project between the Smithsonian Astrophysical Observatory and the Academia Sinica Institute of Astronomy and Astrophysics and is funded by the Smithsonian Institution and the Academia Sinica. We thank the anonymous referee for a very careful and constructive report. We also would like to thank Gaele Dumas for very useful discussion on and help with the kinematic analysis of the  $^{12}\text{CO}$  data. I.S. acknowledges grant LC06014 of Ministry of Education of the Czech Republic. ABP thanks the National Radio Astronomy Observatory (NRAO) for support on this project. NRAO is a facility of the National Science Foundation operated under cooperative agreement by Associated Universities, Inc. SM is supported by the National Science Council (NSC) of Taiwan, NSC 97-2112-M-001-021-MY3.

<sup>17</sup> Please note that we consider the two highest contours in Fig. 22 as being acceptable solutions

## REFERENCES

- Aalto, S., 2008, *Ap&SS*, 313, 273  
 Antonucci, R. R. J., & Miller, J. S. 1985, *ApJ*, 297, 621  
 Ao, Y., Henkel, C., Braatz, J. A., Wei, A., Menten, K. M., Mhle, S., 2011, *A&A*, 529, 154  
 Baum, S.A., Heckman, T.M., van Breugel W., 1992, *ApJ*, 389, 208  
 Blake, G. A., Sutton, E. C., Masson, C. R., & Phillips, T. G., 1987, *ApJ*, 315, 621  
 Bland-Hawthorn, J., Gallimore, J. F., Tacconi, L. J., Brinks, E., Baum, S. A., Antonucci, R. R. J., & Cecil, G. N. 1997, *Ap&SS*, 248, 9  
 Bock, J. J., et al., 2000, *AJ*, 120, 2904  
 Cotton, W. D., Jaffe, W., Perrin, G., Woillez, J., 2008, *A&A*, 477, 517  
 Dale, D.A., Sheth, K., Helou, G., Regan, M.W., Hüttemeister, S., 2005, *AJ*, 129, 2197  
 Fuente, A., García-Burillo, S., Gerin, M., Teyssier, D., Usero, A., Rizzo, J. R., de Vicente, P., 2005, *ApJ*, 619, L155  
 Galliano, E., Pantin, E., Alloin, D., Lagage, P. O., 2005, *MNRAS*, 363, L1  
 Galliano, E., Alloin, D., 2002, *A&A*, 393, 43  
 Gallimore, J.F., Baum, S.A., O'Dea, C.P., 2004, *ApJ*, 613, 794  
 Gallimore, J.F., Henkel, C., Baum, S.A., Glass, I.S., Claussen, M.J., Prieto, M.A., & von Kapherr, A., 2001, *ApJ*, 556, 694  
 Gallimore, J. F., Baum, S. A., & O'Dea, C. P. 1996, *ApJ*, 464, 198  
 Gao, Y., Solomon, Philip M., 2004, *ApJ*, 606, 271  
 García-Burillo, S., et al., 2010, *A&A*, 519, 2  
 García-Burillo, S., Combes, F., Usero, A., Graciá-Carpio, J., 2008, *J. Phys.: Conf. Ser.* 131, 2031  
 García-Burillo, S., Combes, F., Usero, A., Graciá-Carpio, J., 2007, *NewAR*, 51, 160  
 Greenhill, L. J., Gwinn, C. R., Antonucci, R., Barvainis, R., 1996, *ApJ*, 472, L21  
 Greve, T. R., Papadopoulos, P. P., Gao, Y., Radford, S. J. E., 2009, *ApJ*, 692, 1432  
 Guilloteau, S. & Lucas, R. 2000, in *Imaging at Radio Through Submillimeter Wavelengths*, ed. J. G. Mangum & S. J. E. Radford (San Francisco: ASP), 299  
 Heckmann, T.M., Baum, S.A., van Breugel, W.J.M., McCarthy, P., 1989, *ApJ*, 338, 48  
 Henkel, C., Downes, D., Weiß, A., Riechers, D., Walter, F., 2010, *A&A*, 516, 111  
 Henkel, C., Chin, Y.-N., Mauersberger, R., Whiteoak, J. B., 1998, *A&A*, 329, 443  
 Henkel, C., Whiteoak, J. B., Mauersberger, R., 1994, *A&A*, 284, 17  
 Henkel, C., Mauersberger, R., Wiklind, T., Huettemeister, S., Lemme, C., Millar, T. J., 1993, *A&A*, 268, L17  
 Henkel, C. & Mauersberger, R., 1993, *A&A*, 274, 730

TABLE 1  
PROPERTIES OF NGC 1068

Characteristic	NGC 1068	Reference
Hubble Class .....	(R)SA(rs)b	NED <sup>a</sup>
AGN type.....	Seyfert 2	Khachikian & Weedman (1974)
Dynamical Center ..	$\alpha_{J2000}=02h42m40.70s$ $\delta_{J2000}=-00^{\circ}00'47''.9$	Gallimore et al. (2004)
Redshift.....	0.00379 $\pm$ 0.00001	Huchra et al. (1999)
Systemic Velocity ..	(1137 $\pm$ 3)km s <sup>-1</sup>	Huchra et al. (1999)
Luminosity Distance	12.6 Mpc <sup>b</sup>	NED <sup>a</sup>
Scale.....	61 pc/arcsec	NED <sup>a,b</sup>
Inclination Angle...	40 $^{\circ}$	Bland-Hawthorn et al. (1997)
Position Angle .....	278 $^{\circ}$	Bland-Hawthorn et al. (1997)

<sup>a</sup> NED: NASA/IPAC Extragalactic Database

<sup>b</sup> Used cosmology: Hubble constant  $H_0 = 73$  km s<sup>-1</sup>/Mpc,  $\Omega(\text{matter}) = 0.27$ ,  $\Omega(\text{vacuum}) = 0.73$

- Hoening, S.F., Almudena Prieto, M., Beckert, Th., 2008, *A&A*, 485, 33
- Huchra, J. P., Vogeley, M. S., & Geller, M. J. 1999, *ApJS*, 121, 287
- Humphreys, E. M. L., Greenhill, L. J., Reid, M. J., Beuther, H., Moran, J. M., Gurwell, M., Wilner, D. J., & Kondratko, P. T. 2005, *ApJ*, 634, L133
- Irvine, W. M., Goldsmith, P. F., Hjalmarsen, A., in *Interstellar processes, Proceedings of the Symposium, Grand Teton National Park, WY, July 1-7, 1986 (A88-14501 03-90)*. Dordrecht, D. Reidel Publishing Co., 1987, *ASSL* 134, p. 561-609
- Israel, F.P., 2009, *A&A*, 493, 525
- Jaffe, W., et al., 2004, *Natur*, 429, 47
- Kamenetzky, J., et al., 2011, *ApJ*, 731, 83
- Khachikian, E. Y., & Weedman, D. W. 1974, *ApJ*, 192, 581
- Kohno, K., Nakanishi, K., Tosaki, T., Muraoka, K., Miura, R., Ezawa, H., Kawabe, R., 2008, *Ap&SS*, 313, 279
- Kohno, K., Matsushita, S., Vila-Vilaró, B., Okumura, S. K., Shibatsuka, T., Okiura, M., Ishizuki, S., & Kawabe, R. 2001, in *ASP Conf. Ser. 249, The Central kpc of Starbursts and AGN*, ed. J. H. Knapen et al. (San Francisco: ASP), 672
- Kohno, K., Kawabe, R., Tosaki, T., Okumura, S., 1996, *ApJ*, 461, L29
- Kraemer, S.B., Ruiz, J.R., Crenshaw, D. M., 1998, *ApJ*, 508, 232
- Krips, M., Martín, S., Neri, R., García-Burillo, S., Combes, F., Petitpas, G., Fuente, A., Usero, A., "The Starburst-AGN Connection", *ASP Conference Series*, Vol. 408, proc. of the conference held 27-31 October 2008, at Shanghai Normal University, Shanghai, China. Edited by Weimin Wang, Zhaoqing Yang, Zhijian Luo, and Zhu Chen. San Francisco: Astronomical Society of the Pacific, 2009, p.142
- Krips, M., Neri, R., García-Burillo, S., Martín, S., Combes, F., Graciá-Carpio, J., Eckart, A., 2008, *ApJ*, 677, 262
- Krips, M., et al., 2007, *A&A*, L468
- Krips, M., et al., 2006, *A&A*, 446, 113
- Krolik, J. H., & Kallman, T. R. 1987, *ApJ*, 320, L5
- Martín, S., et al., 2011, *A&A*, 527, 36
- Martín, S., Aladro, R., Martín-Pintado, J., Mauersberger, R., 2010, *A&A*, 522, 62
- Martín, S., Mauersberger, R., Martín-Pintado, J., Henkel, C., García-Burillo, S., 2006, *ApJS*, 164, 450
- Meier, David S., Turner, Jean L., 2005, *ApJ*, 618, 259
- Muller, S., Guelin, M., Dumke, M., Lucas, R., Combes, F., 2006, *A&A*, 458, 417
- Müller-Sánchez, F., Davies, R. I., Genzel, R., Tacconi, L. J., Eisenhauer, F., Hicks, E. K. S., Friedrich, S., Sternberg, A., 2009, *ApJ*, 691, 749
- Matsushita, S., Muller, S., Lim, J., 2007, *A&A*, 468, L49
- Matsushita, S., et al., 2004, *ApJ*, 616, L55
- Matsushita, S., Kawabe, R., Kohno, K., Matsumoto, H., Tsuru, T.G., Vila-Vilaró, B., 2005, *ApJ*, 618, 712
- Matsushita, S., Kawabe, R., Matsumoto, H., Tsuru, T.G., Kohno, K., Morita, K.-I., Okumura, S.K., Vila-Vilaró, B., 2000, *ApJ*, 545, L107
- Matsushita, S., Kohno, K., Vila-Vilaró, B., Tosaki, T., Kawabe, R., 1998, *ApJ*, 495, 267
- Meijerink, R., Spaans, M., Israel, F. P., 2007, *A&A*, 461, 793
- Meijerink, R., & Spaans, M., 2005, *A&A*, 436, 397
- Naylor, B. J., et al., 2010, *ApJ*, 722, 668
- Paglione, T. A. D., Jackson, J. M., Bolatto, A. D., Heyer, M. H., 1998, *ApJ*, 493, 680
- Papadopoulos, P. P., 2010, *ApJ*, 720, 226
- Pérez-Beaupuits, J. P., Spaans, M., van der Tak, F.F.S., Aalto, S., García-Burillo, S., Fuente, A., Usero, A., 2009, *A&A*, 503, 459
- Poncet, A., Perrin, ., Sol, H., 2008, *A&A*, 481, 305
- Rigopoulou, D., Kunze, D., Lutz, D., Genzel, R., Moorwood, A. F. M., 2002, *A&A*, 389, 374
- Roussel, H., et al., 2007, *ApJ*, 669, 959
- Roy, A.L., Colbert, E.J.M., Wilson, A.S., & Ulvestad, J.S., 1998, *ApJ*, 504, 147
- Sakamoto, K., Aalto, S., Evans, A. S., Wiedner, M.C., Wilner, D. J., 2010, *ApJ*, 725, L228
- Sakamoto, K., Ho, P. T. P., Peck, A. B., 2006, *ApJ*, 644, 862
- Schinnerer, E., Eckart, A., Tacconi, L.J., Genzel, R. & Downes, D., 2000, *ApJ*, 533, 850
- Scoville, N.Z., Carlstrom, J.E., Chandler, C.J., Phillips, J.A., Scott, S.L., Tilanus, R. P.J., Wang, Z., 1993, *PASP*, 105, 1482
- Siemiginowska, A., & Elvis, M., 1997, *ApJ*, 482, L9
- Sternberg, A., Genzel, R., & Tacconi, L. 1994, *ApJ*, 436, L131
- Tacconi, L. J., Genzel, R., Blietz, M., Cameron, M., Harris, A. I., Madden, S., 1994, *ApJ*, 426, L77
- Tomono, D., Terada, H., Kobayashi, N., 2006, *ApJ*, 646, 774
- Usero, A., García-Burillo, S., Martín-Pintado, J., Fuente, A., Neri, R., 2006, *A&A*, 448, 457
- Usero, A., García-Burillo, S., Fuente, A., Martín-Pintado, J., & Rodríguez-Fernández, N. J. 2004, *A&A*, 419, 897
- Van der Tak, F.F.S., Black, J.H., Schöier, F.L., Jansen, D.J., van Dishoeck, E.F. 2007, *A&A* 468, 627
- Wang, M., Henkel, C., Chin, Y.-N., Whiteoak, J. B., Hunt C., M., Mauersberger, R., Muders, D., 2004, *A&A*, 422, 883
- Wilson, T. L. & Rood, R., 1994, *ARA&A*, 32, 191
- Wilson, T. L., & Matteucci, F., 1992, *A&AR* 4, 1

TABLE 2  
CHRONOLOGICAL SUMMARY OF OBSERVATIONS CARRIED OUT FOR NGC 1068

Molecular Line	Telescope	Observing Dates (YYYY-MM)	Config. <sup>a</sup>	Frequency at rest (GHz)	Band	Zenith Opacity at 225 GHz	T <sub>sys</sub> (K)	RMS Noise <sup>b</sup> (mJy)	Synthesized Beam major×minor,P.A. <sup>c</sup> (″×″,°)
<sup>13</sup> CO(J=2-1) & C <sup>18</sup> O(J=2-1)	SMA	2008-01,2008-02	EX	220.399 219.560	LSB LSB	0.10-0.20	100-150	12	1.0×0.8,30 <sup>d</sup>
HCO <sup>+</sup> (J=4-3)	SMA	2007-08,2007-09	EX	356.734	USB	0.06-0.13	200-400	32 <sup>e</sup>	1.0×0.8,30 <sup>f</sup>
<sup>12</sup> CO(J=3-2)	SMA	2007-09	EX	345.796	LSB	0.06-0.13	200-400	51	1.0×0.8,30 <sup>f</sup>
HCO <sup>+</sup> (J=3-2)	SMA	2006-11	EX	267.558	LSB	0.06-0.15	100-150	33	1.0×0.8,30 <sup>f</sup>
HCN(J=3-2)	SMA	2006-01	EX	265.886	LSB	0.05-0.10	100-150	24 <sup>e</sup>	1.0×0.8,30 <sup>e,f</sup>
	SMA	2006-10,2006-11	VEX		LSB	0.10-0.22	100-200		0.53×0.46,30 <sup>d,e</sup>
<sup>13</sup> CO(J=3-2)	SMA	2005-10	C	356.734	USB	0.05-0.06	200-300	39	2.4×2.1,28 <sup>d</sup>
<sup>13</sup> CO(J=1-0)	PdBI	2003-02	A	110.201	SSB	n.a.	150-300	1.7	2.5×1.9,28 <sup>f</sup>
<sup>12</sup> CO(J=2-1)	PdBI	2003-02	A	230.538	SSB	n.a.	200-600	4	1.0×0.8,30 <sup>e</sup>

<sup>a</sup> SMA configurations: C=compact (baselines up to 70 m), EX=extended (baselines up to 220 m), VEX=very extended (baselines up to 500 m); PdBI configurations: A=most extended (baselines up to 500m)

<sup>b</sup> in 17 km s<sup>-1</sup> wide channels

<sup>c</sup> P.A. is measured from North to East

<sup>d</sup> using uniform weighting

<sup>e</sup> combined for all tracks

<sup>f</sup> using natural weighting

TABLE 3  
CONTINUUM PARAMETERS FOR NGC 1068.

λ	Synth. Beam major×minor,P.A. (″×″,°)	Δα <sup>a</sup> (″)	Δδ <sup>a</sup> (″)	Peak Flux (mJy/beam)	Flux Density <sup>b</sup> (mJy)	Deconv. Size major×minor,P.A. (″×″,°)
1.4 mm	1.0×0.8,30	+0.13±0.02	+0.25±0.02	19±2	28±3	(0.9±0.1)×(0.7±0.1),(50±20)
1.3 mm	1.0×0.8,30	+0.18±0.02	+0.23±0.02	15±1	22±2	(0.6±0.1)×(0.5±0.1),(40±20)
1.0 mm (NA) <sup>c</sup>	1.0×0.8,30	+0.17±0.05	+0.15±0.10	19±2	24±3	(0.8±0.1)×(0.4±0.1),(20±10)
1.0 mm (UN) <sup>d</sup>	0.5×0.4,30	+0.13±0.03	+0.07±0.03	12±2	13±2	(0.3±0.1) <sup>e</sup>
810 μm	2.1×2.0,80	-0.04±0.2	-0.07±0.2	30±4	41±11	(1.1±0.1)×(0.8±0.2),(90±20)
850 μm (NA)	1.0×0.8,30	+0.33±0.07	+0.05±0.06	24±2	50±7	(1.1±0.1)×(0.8±0.2),(90±20)
850 μm (UN)	0.6×0.5,30	+0.33±0.09	-0.03±0.07	16±3	30±5	(1.1±0.1)×(0.8±0.2),(90±20)

<sup>a</sup> The offsets are with respect to α<sub>J2000</sub> =02h42m40.70s and δ<sub>J2000</sub> =-00°00′47″.9 which is almost identical to the radio position of the AGN in NGC 1068 of α<sub>J2000</sub> =02h42m40.709s and δ<sub>J2000</sub> =-00°00′47″.95 (e.g. Gallimore et al. 2004; Krips et al. 2006). Positional errors are of pure statistical nature and were derived from the Gaussian fit to the data. They do not include absolute positional uncertainties from the calibration, which are estimated to be ~0″.1.

<sup>b</sup> Flux errors are purely statistical and do not account for uncertainties of the flux calibration. The latter are estimated to be of the order 10-20% (see text).

<sup>c</sup> Averaged continuum emission derived from the HCN(J=3-2) (vex+ext) and HCO<sup>+</sup>(J=3-2) observations (ext). Data were mapped using natural weighting (NA).

<sup>d</sup> Averaged continuum emission derived from the HCN(J=3-2) observations alone (vex+ext) using uniform weighting (UN).

<sup>e</sup> Here, only a circular Gaussian fit has been carried out, while for the rest an elliptical Gaussian has been fitted to the data (see text).

TABLE 4  
 INDIVIDUAL COMPONENTS OF THE MOLECULAR LINE EMISSION IN NGC 1068.

Molecular Line	Component	$\Delta\alpha^a$ ( $''$ )	$\Delta\delta^a$ ( $''$ )	Vel. Integrated Peak Intensity <sup>a</sup> (Jy beam <sup>-1</sup> km s <sup>-1</sup> )	Spatially Integrated Intensity <sup>a</sup> (Jy km s <sup>-1</sup> )
HCN(J=3-2)	E-knot	+1.0±0.1	+0.1±0.1	51±8	110±20
	W-knot	-0.8±0.2	+0.2±0.2	32±4	70±10
HCO <sup>+</sup> (J=3-2)	E-knot	+0.9±0.1	+0.0±0.1	28±5	52±5
	W-knot	-0.8±0.2	+0.5±0.2	14±2	40±5
HCO <sup>+</sup> (J=4-3)	E-knot	+0.9±0.1	+0.1±0.1	27±6	98±20
<sup>12</sup> CO(J=3-2)	E-knot	+1.1±0.1	-0.1±0.1	470±20	1330±200
	W-knot	-1.2±0.1	-0.1±0.1	270±10	720±100
<sup>13</sup> CO(J=3-2)	E-knot	+1.1±0.1	+0.3±0.1	24±3	40±10
<sup>12</sup> CO(J=2-1)	E-knot	+1.0±0.1	-0.2±0.1	70±10	290±20
	W-knot	-1.3±0.1	-0.3±0.1	30±5	180±20
<sup>13</sup> CO(J=2-1)	E-knot	+0.6±0.2	+0.4±0.2	10±2	18±3
	W-knot	-1.2±0.3	+0.1±0.1	8±2	16±3
C <sup>18</sup> O(J=2-1)	E-knot	+0.3±0.3	+0.5±0.3	7±1	15±3
<sup>13</sup> CO(J=1-0)	E-knot	+1.0±0.4	-0.4±0.4	0.4±0.2	0.5±0.2
	W-knot	-1.3±0.4	-0.8±0.5	0.4±0.2	0.5±0.2
<sup>12</sup> CO(J=1-0)	E-knot	+0.5±0.1	+0.1±0.1	40±1	90±2
	W-knot	-1.1±0.1	-0.5±0.1	19±1	40±2

<sup>a</sup> The parameters were determined by fitting a one- or two-component elliptical Gaussian profile to the  $uv$ -data of each line. Errors include the statistical uncertainties from the Gaussian fit and those from the calibration ( $\sim 10$ -20%). Offsets are with respect to the center position specified in Table 3.

 TABLE 5  
 MOLECULAR LINE PARAMETERS DERIVED FROM THE DIFFERENT LINE SPECTRA OF NGC 1068.

Molecular Line	Velocity Offset <sup>a,b,c</sup> (km s <sup>-1</sup> )	Line Flux <sup>a</sup> (Jy)	Line Width <sup>a,b,d</sup> (km s <sup>-1</sup> )	Vel. Integrated Intensity <sup>a,b</sup> (Jy km s <sup>-1</sup> )	Vel. Integrated SD Intensity <sup>e</sup> (Jy km s <sup>-1</sup> )	SD Beam ( $''$ )
HCN(J=3-2)	-30±10	0.63±0.08	200±30	150±10	190±10	9.5 $''$
HCO <sup>+</sup> (J=3-2)	-40±10	0.23±0.03	190±50	50±6	80±8	9.5 $''$
HCO <sup>+</sup> (J=4-3)	-40±10	0.24±0.03	240±40	60±6	70±10	14 $''$
<sup>12</sup> CO(J=3-2)	-30±3	12.3±0.40	170±10	2130±5	2600±300	14 $''$
<sup>13</sup> CO(J=3-2)	-40±10	0.43±0.03	230±30	100±10	170±20	14 $''$
<sup>12</sup> CO(J=2-1)	-30±6	2.20±0.10	230±20	529±2	950±6	12 $''$
<sup>13</sup> CO(J=2-1)	-10±10	0.50±0.04	60±10	30±1	55±7	12 $''$
C <sup>18</sup> O(J=2-1)	+3±10	0.10±0.02	50±10	5.1±0.3	...	...
<sup>12</sup> CO(J=1-0)	+3±2	0.50±0.02	240±10	120±4	650±80	21 $''$
<sup>13</sup> CO(J=1-0)	+8±10	0.009±0.002	140±30	1.3±0.3	56±7	21 $''$

<sup>a</sup> The line parameters have been determined by fitting a single Gaussian line to the (spatially integrated) spectrum for each molecule. The line emission has been thereby integrated over the central 4 $''$  in NGC 1068.

<sup>b</sup> statistical error from the Gaussian fit only.

<sup>c</sup> with respect to  $v_{\text{LSR}}=1137$  km/s.

<sup>d</sup> Full Width at Half Maximum (FWHM)

<sup>e</sup> single dish (SD) integrated intensities as measured with the IRAM 30m and the JCMT telescope in the central 10-30 $''$  of NGC 1068 (taken from: Israel 2009; Pérez-Beaupuits et al. 2009; Krips et al. 2008). The values were converted to Jansky scale using  $S[\text{Jy}]/T_{\text{mb}}[\text{K}]=4.71$  (30m) and  $S[\text{Jy}]/T_{\text{mb}}[\text{K}]=15.6$  (JCMT).

TABLE 6  
MOLECULAR LINE RATIOS FOR NGC 1068<sup>a</sup>. (X[K]/Y[K])

X	Y	<sup>12</sup> CO			<sup>13</sup> CO			<sup>C</sup> <sup>18</sup> O		HCN		HCO <sup>+</sup>		
		J=1-0	J=2-1	J=3-2	J=1-0	J=2-1	J=3-2	J=2-1	J=1-0	J=2-1	J=3-2	J=1-0	J=3-2	J=4-3
E-knot														
<sup>12</sup> CO	J=1-0	...	0.3±0.2	0.2±0.1	20±10	...	...	...	...	...	...	...	...	...
	J=2-1	2.9±0.3	...	0.3±0.2	...	5.0±3.0	...	17±4	...	...	4.0±2.0	...	7.0±3.0	...
	J=3-2	6.0±3.0	4.0±2.0	...	...	...	25±6	...	...	...	5.0±3.0	...	8.0±3.0	...
<sup>13</sup> CO	J=1-0	0.05±0.03	...	...	...	0.2±0.1	0.08±0.04	...	...	...	...	...	...	...
	J=2-1	...	0.2±0.1	...	5.0±3.0	...	0.7±0.3	1.4±0.3	...	...	0.3±0.2	...	0.5±0.2	...
	J=3-2	...	...	0.04±0.01	13±4	1.4±0.4	...	...	...	...	0.2±0.1	...	0.5±0.3	...
<sup>C</sup> <sup>18</sup> O	J=2-1	...	0.06±0.03	...	...	0.8±0.3	...	...	...	...	...	...	...	...
	J=3-2	...	...	...	...	...	...	...	...	...	...	...	...	...
HCN	J=1-0	...	...	...	...	...	...	...	...	...	...	...	...	...
	J=3-2	...	0.3±0.1	0.14±0.03	...	4±1	4.0±1.0	...	...	...	...	...	...	...
HCO <sup>+</sup>	J=1-0	...	...	...	...	...	...	...	...	...	...	...	...	...
	J=3-2	...	0.13±0.02	0.07±0.01	...	2.0±0.4	2.0±0.5	...	...	...	0.6±0.3	...	...	1.8±0.9
	J=4-3	...	...	...	...	...	...	...	...	...	...	...	0.6±0.3	...
W-knot														
<sup>12</sup> CO	J=1-0	...	0.8±0.7	0.3±0.2	50±30	...	...	...	...	...	...	...	...	...
	J=2-1	1.5±0.5	...	0.3±0.2	...	10±2	...	...	...	...	3.4±0.6	...	6.0±1.0	...
	J=3-2	4.0±2.0	3.0±2.0	...	...	...	25±6	...	...	...	6.0±1.0	...	11±2	...
<sup>13</sup> CO	J=1-0	0.02±0.01	...	...	...	0.13±0.06	...	...	...	...	...	...	...	...
	J=2-1	...	0.10±0.02	...	8.0±4.0	...	...	...	...	...	0.4±0.2	...	0.6±0.3	...
	J=3-2	...	...	0.04±0.01	...	...	...	...	...	...	...	...	...	...
<sup>C</sup> <sup>18</sup> O	J=2-1	...	...	...	...	...	...	...	...	...	...	...	...	...
	J=3-2	...	...	...	...	...	...	...	...	...	...	...	...	...
HCN	J=1-0	...	...	...	...	...	...	...	...	...	...	...	...	...
	J=3-2	...	0.3±0.1	0.2±0.1	...	3.0±2	...	...	...	...	...	...	1.9±0.5	...
HCO <sup>+</sup>	J=1-0	...	...	...	...	...	...	...	...	...	...	...	...	...
	J=3-2	...	0.17±0.03	0.09±0.02	...	1.7±0.4	...	...	...	...	0.5±0.3	...	...	...
	J=4-3	...	...	...	...	...	...	...	...	...	...	...	...	...
Total														
<sup>12</sup> CO	J=1-0	...	0.3±0.2	0.3±0.2	40±20	...	...	...	...	...	...	...	...	...
	J=2-1	2.0±1.0	...	0.3±0.2	...	8±3	...	94±6	...	...	4.0±2.0	...	9.0±4.0	...
	J=3-2	4.0±2	4.0±2.0	...	...	...	41±2.0	...	...	...	8.0±4.0	...	16±1	...
<sup>13</sup> CO	J=1-0	0.04±0.02	...	...	...	0.17±0.04	0.2±0.1	...	...	...	...	...	...	...
	J=2-1	...	0.2±0.1	...	6.0±1.0	...	1.0±0.5	...	...	...	0.3±0.2	...	0.6±0.3	...
	J=3-2	...	...	0.025±0.001	4.0±1.0	0.7±0.3	...	...	...	...	0.2±0.1	...	0.4±0.2	...
<sup>C</sup> <sup>18</sup> O	J=2-1	...	0.011±0.001	...	...	0.2±0.1	...	...	...	...	...	...	...	...
	J=3-2	...	...	...	...	...	...	...	...	...	...	...	...	...
HCN	J=1-0	...	...	...	...	...	...	...	...	...	...	...	...	...
	J=3-2	...	0.3±0.1	0.12±0.01	...	3.0±0.3	5.0±3.0	...	...	...	...	...	1.9±0.2	...
HCO <sup>+</sup>	J=1-0	...	...	...	...	...	...	...	...	...	...	...	...	...
	J=3-2	...	0.11±0.01	0.08±0.02	...	1.8±0.1	3.0±0.2	...	...	...	0.5±0.3	...	...	1.6±0.8
	J=4-3	...	...	...	...	...	1.6±0.1	...	...	...	...	...	0.6±0.3	...

<sup>a</sup> The line ratios were derived by spatially averaging over the respective region from the velocity intergrated line ratio maps from Fig. 12. The errors denote thereby the standard deviation from the averaged values. Please note, that in some cases, the line ratios might vary from those estimated from Tables 4 and 5. See text for a discussion.

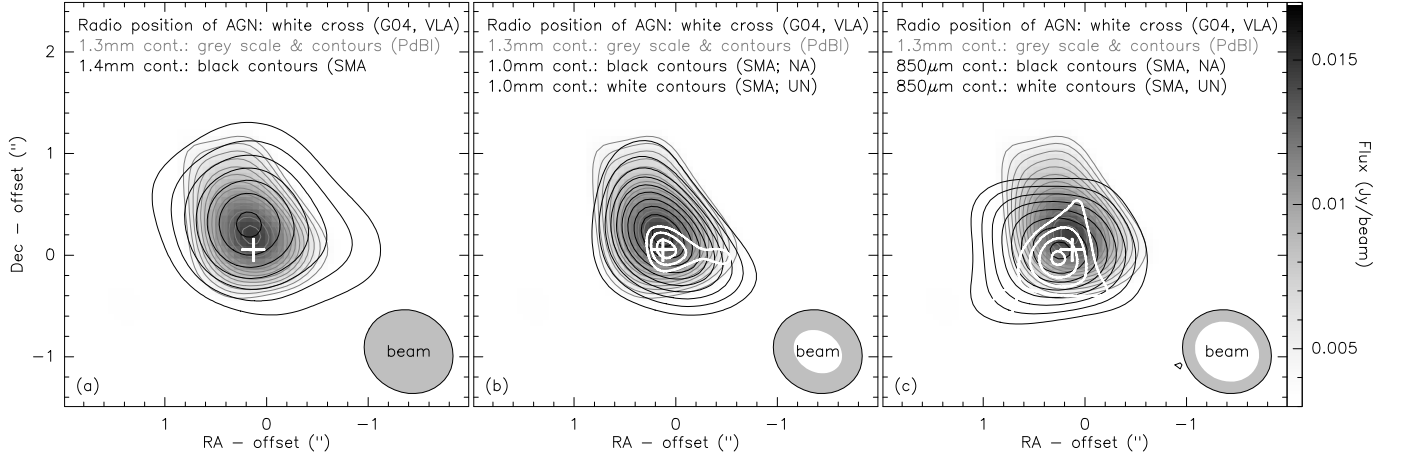


FIG. 1.— Continuum emission of NGC 1068 at  $\lambda=1.4$  mm (Fig. 1a; black contours), 1.3 mm (Fig. 1a-c; grey scale and grey contours), 1.0 mm (Fig. 1b; black contours) and 850  $\mu\text{m}$  (Fig. 1c; black contours), observed with the SMA and the IRAM PdBI. The white cross denotes the position of the AGN measured by Gallimore et al. (2004, G04). The contours of the 1.3 mm continuum emission (PdBI) start at  $5\sigma=4$  mJy in steps of  $1\sigma$ . *a*) The contours of the 1.4 mm continuum emission (SMA) start at  $5\sigma=4$  mJy in steps of  $1\sigma$ . *b*) The contours of the 1.0 mm continuum emission (SMA, NA) start at  $3\sigma=1.6$  mJy in steps of  $1\sigma$ , while the contours of the uniformly mapped 1.0 mm continuum emission run from  $3\sigma=2.3$  mJy in steps of  $1\sigma$ . *c*) The contours of the 850  $\mu\text{m}$  continuum emission (SMA, NA) start at  $3\sigma=2.4$  mJy in steps of  $1\sigma$ , while the contours of the uniformly mapped 850  $\mu\text{m}$  continuum emission run from  $3\sigma=2.6$  mJy in steps of  $1\sigma$ .

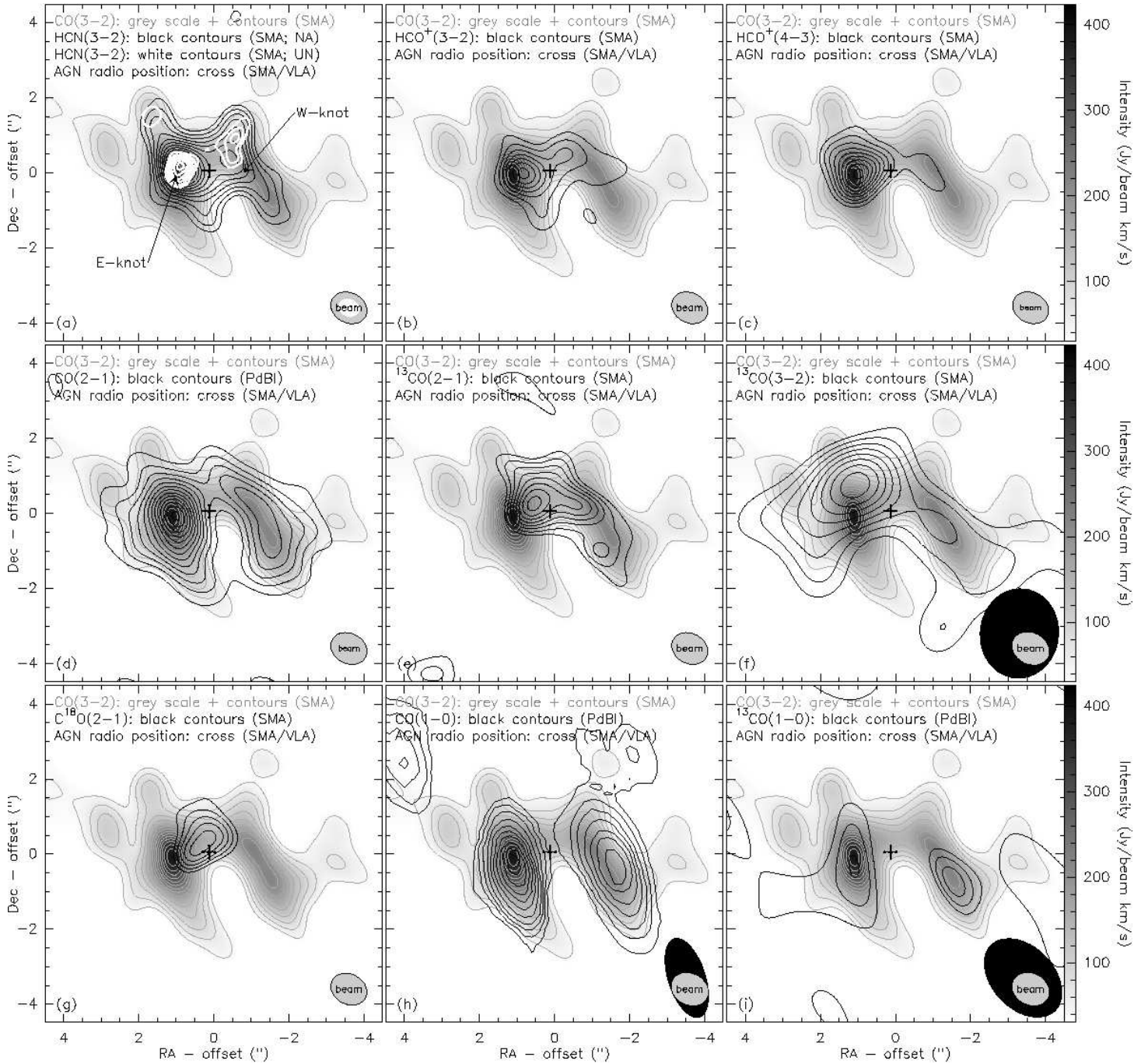


FIG. 2.— Velocity integrated line emission of  $^{12}\text{CO}(J=3-2)$  (a-g),  $\text{HCN}(J=3-2)$  (a),  $\text{HCO}^+(J=3-2)$  (b),  $\text{HCO}^+(J=4-3)$  (c),  $^{12}\text{CO}(J=2-1)$  (d),  $^{13}\text{CO}(J=2-1)$  (e),  $^{13}\text{CO}(J=3-2)$  (f),  $\text{C}^{18}\text{O}(J=2-1)$  (g),  $^{12}\text{CO}(J=1-0)$  (h) and  $^{13}\text{CO}(J=1-0)$  (i) in NGC 1068, observed with the SMA and the IRAM PdBI. Contour levels are:  $^{12}\text{CO}(J=3-2)$  – from  $10\sigma$  by  $6\sigma$  with  $1\sigma=4.8 \text{ Jy km s}^{-1}$ ;  $\text{HCN}(J=3-2)$  – from  $3\sigma$  by  $1\sigma$  with  $1\sigma=2.6 \text{ Jy km s}^{-1}$ ;  $\text{HCO}^+(J=3-2)$  – from  $2\sigma$  by  $1\sigma$  with  $1\sigma=3.4 \text{ Jy km s}^{-1}$ ;  $\text{HCO}^+(J=4-3)$  – from  $3\sigma$  by  $1\sigma$  with  $1\sigma=2.4 \text{ Jy km s}^{-1}$ ;  $^{12}\text{CO}(J=2-1)$  – from  $5\sigma$  by  $5\sigma$  with  $1\sigma=1.2 \text{ Jy km s}^{-1}$ ;  $^{13}\text{CO}(J=2-1)$  – from  $3\sigma$  by  $1\sigma$  with  $1\sigma=0.9 \text{ Jy km s}^{-1}$ ;  $^{13}\text{CO}(J=3-2)$  – from  $5\sigma$  by  $1\sigma$  with  $1\sigma=3.5 \text{ Jy km s}^{-1}$ ;  $\text{C}^{18}\text{O}(J=2-1)$  – from  $3\sigma$  by  $1\sigma$  with  $1\sigma=0.9 \text{ Jy km s}^{-1}$ ;  $^{12}\text{CO}(J=1-0)$  – from  $5\sigma$  by  $3\sigma$  with  $1\sigma=0.4 \text{ Jy km s}^{-1}$ ;  $^{13}\text{CO}(J=1-0)$  – from  $1\sigma$  by  $1\sigma$  with  $1\sigma=0.1 \text{ Jy km s}^{-1}$ .

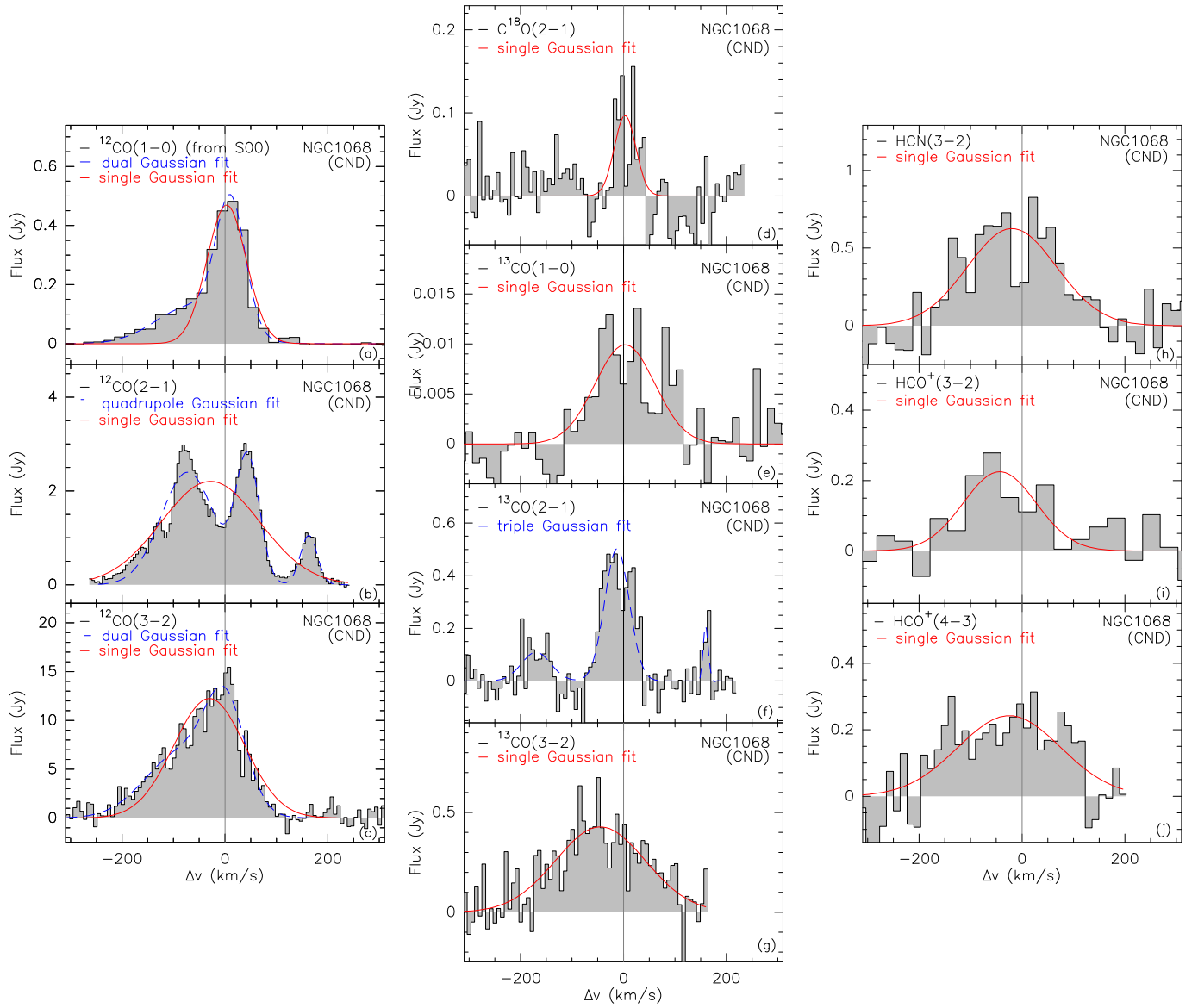


FIG. 3.— Spatially integrated spectrum of different molecular lines in NGC 1068. The single-line Gaussian fit is indicated with a dotted red line (parameters are listed in Table 5) while the multiple Gaussian fit is plotted with a dashed blue line.

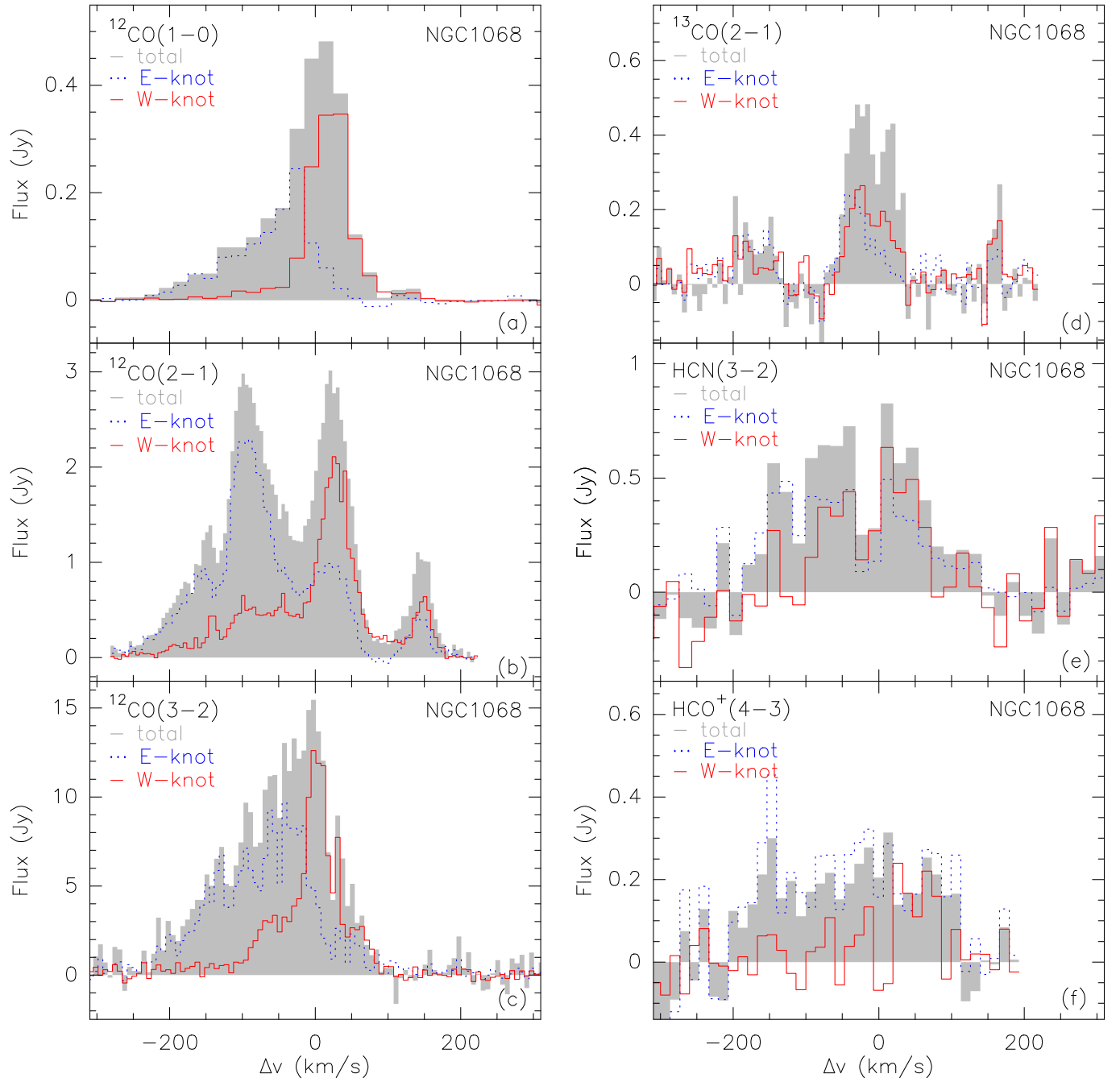


FIG. 4.— Spatially integrated spectrum of the  $^{12}\text{CO}(J=1-0)$ , (taken from Schinnerer et al. 2000),  $^{12}\text{CO}(J=2-1)$  and  $^{12}\text{CO}(J=3-2)$  (left column) and  $\text{HCN}(J=3-2)$  and  $\text{HCO}^+(J=4-3)$  emission over the E-knot (dotted blue) and W-knot (solid red) component of NGC 1068.

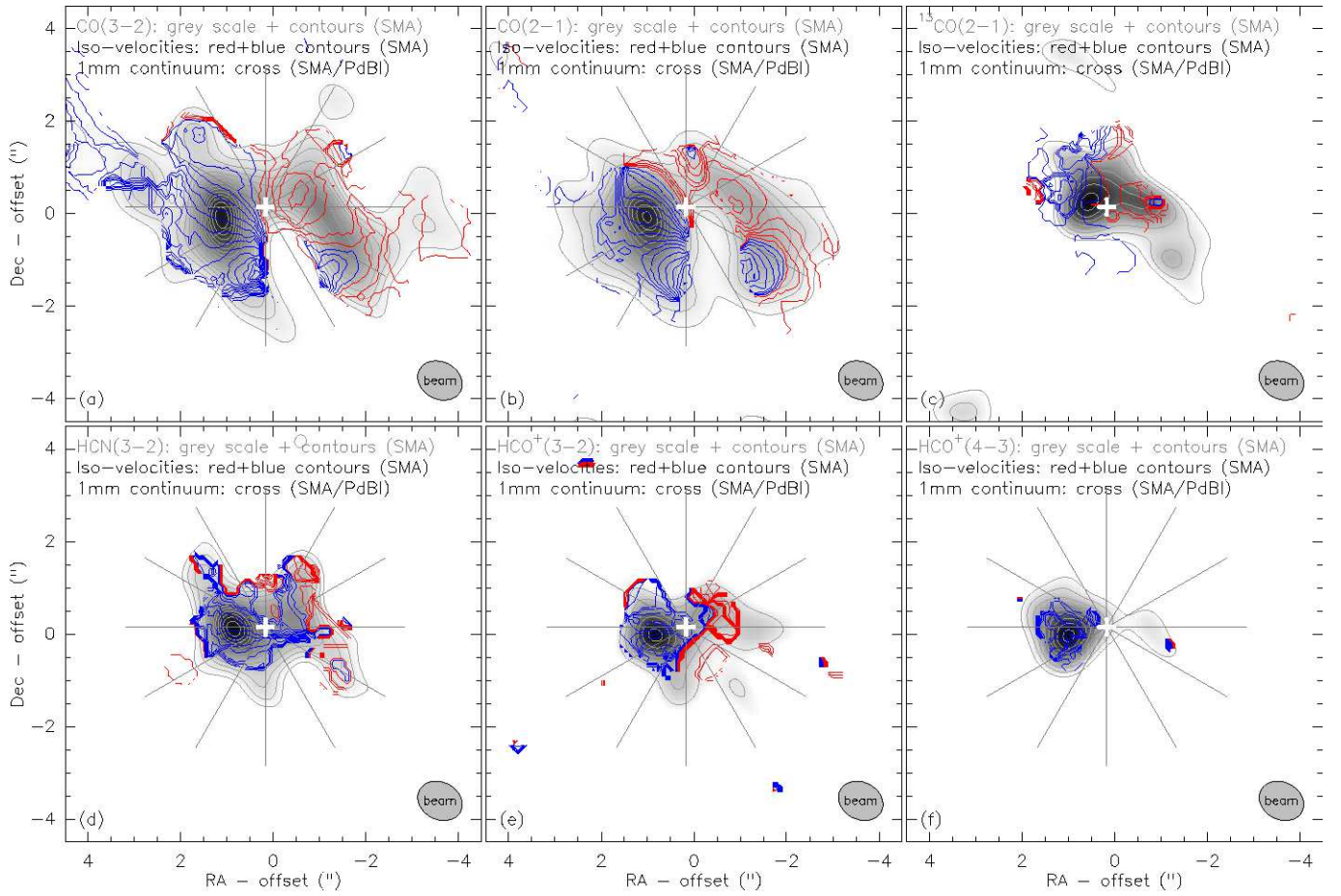


FIG. 5.— Iso-velocity maps of the different molecular lines observed in NGC 1068. The grey scale correspond to the velocity integrated emission of each line with the same contours as used in Fig. 2. The velocity contours are in steps of  $10 \text{ km s}^{-1}$  around the systemic velocity of NGC 1068. The grey lines indicate the cuts along which the position-velocity diagrams (see Fig. 10) were taken for the respective molecules ( $^{12}\text{CO}(J=2-1)$ ,  $^{12}\text{CO}(J=2-1)$  &  $\text{HCN}(J=3-2)$ ).

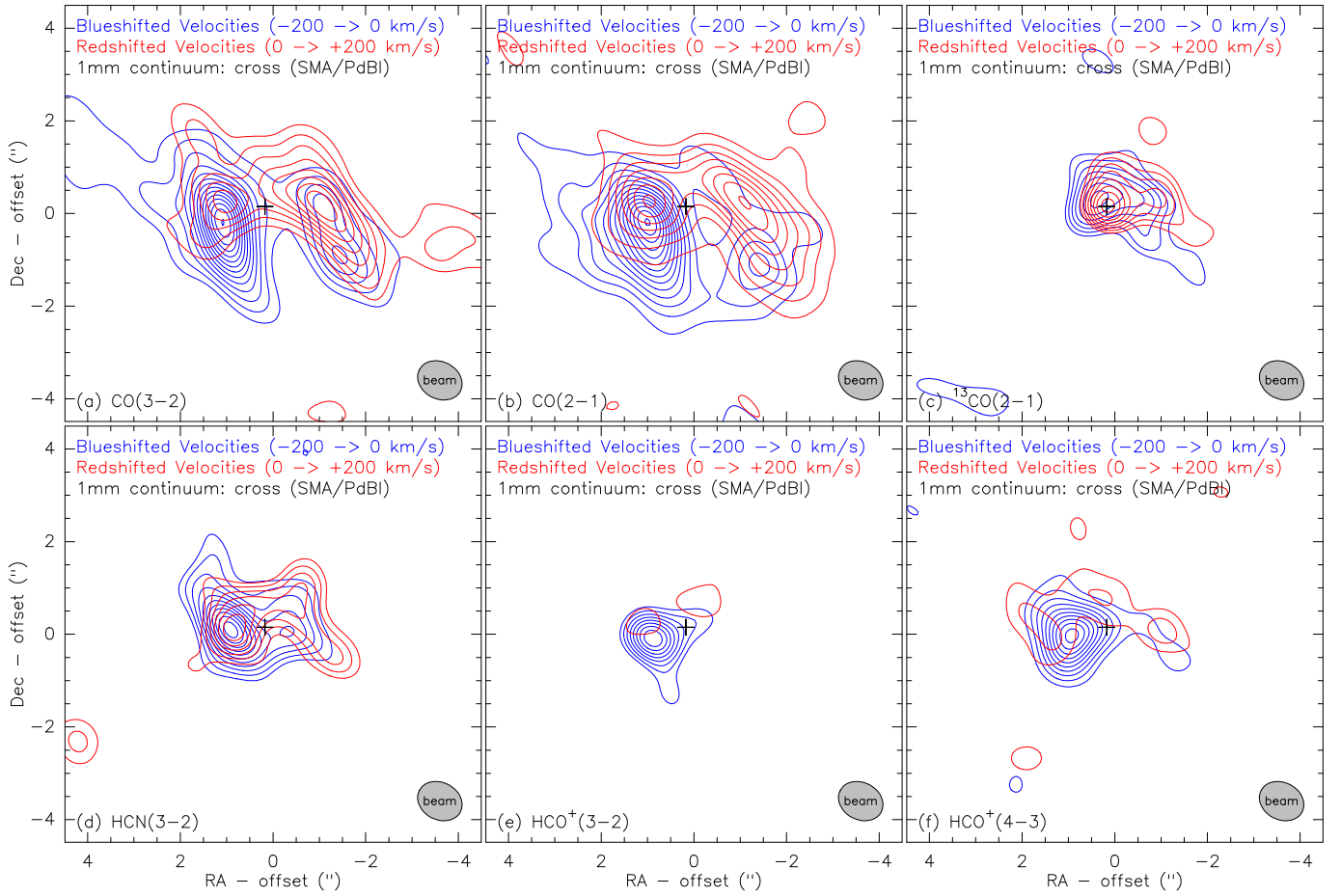


FIG. 6.— Red- and blueshifted emission of NGC1068. Contours are in steps of a) from  $7\sigma$  by  $5\sigma$  with  $1\sigma=2.0 \text{ Jy km s}^{-1}$ ; b) from  $5\sigma$  by  $5\sigma$  with  $1\sigma=0.9 \text{ Jy km s}^{-1}$ ; c) from  $4\sigma$  by  $1\sigma$  with  $1\sigma=0.5 \text{ Jy km s}^{-1}$ ; d) from  $3\sigma$  by  $1\sigma$  with  $1\sigma=1.9 \text{ Jy km s}^{-1}$ ; e) from  $3\sigma$  by  $1\sigma$  with  $1\sigma=2.3 \text{ Jy km s}^{-1}$ ; f) from  $2\sigma$  by  $1\sigma$  with  $1\sigma=1.4 \text{ Jy km s}^{-1}$ .

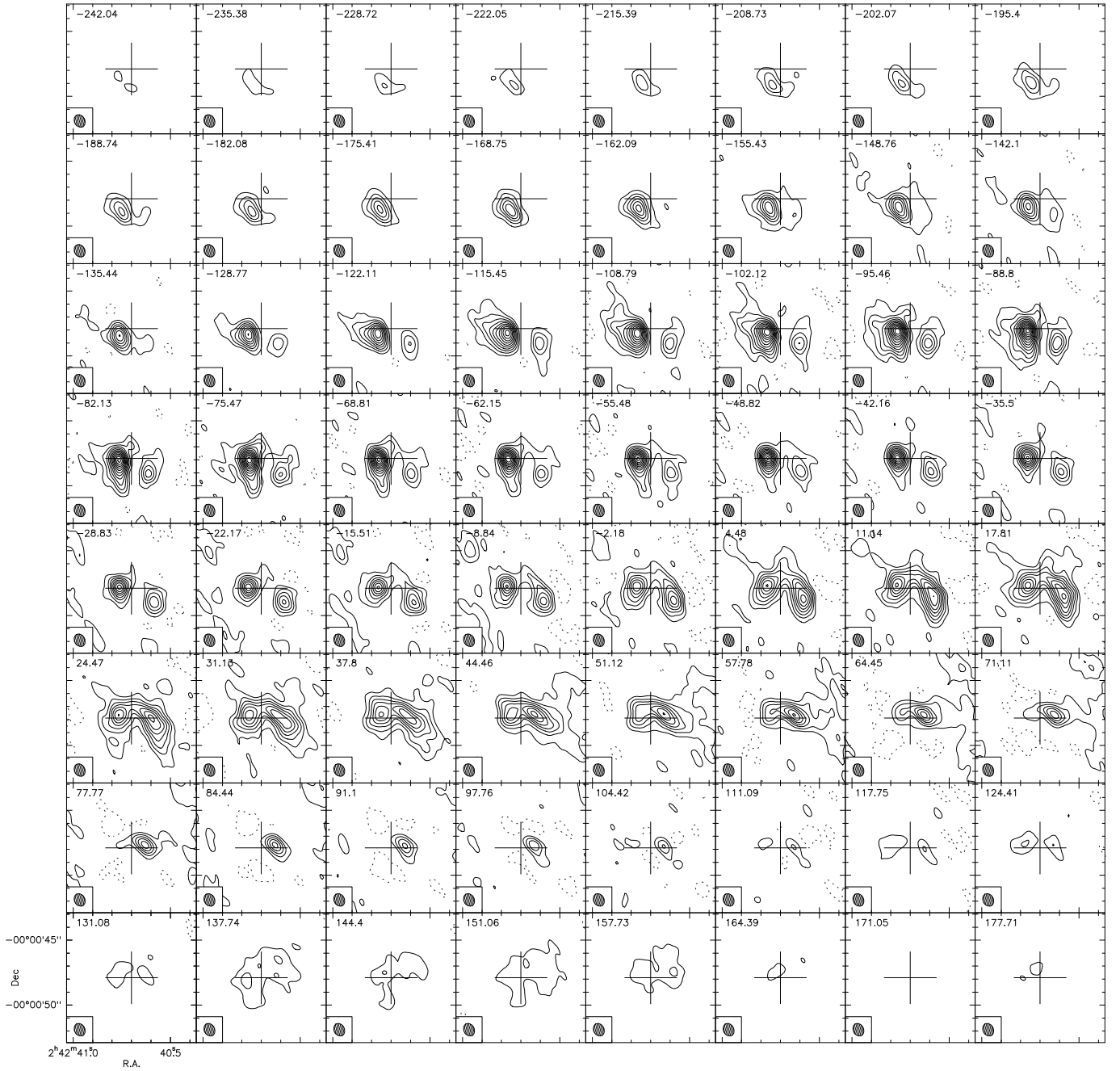


FIG. 7.— Channel maps of the  $^{12}\text{CO}(J=2-1)$  emission in NGC 1068. Please note that the  $^{12}\text{CO}(J=2-1)$  data were resampled to match the spectral resolution of the  $^{12}\text{CO}(J=3-2)$  data and facilitate a comparison, especially with respect to the line-ratio channel map in Fig. 13. Contour spacing is in steps of  $5\sigma=37.4 \text{ mJy beam}^{-1}$ . We use a spectral resolution of  $\sim 7 \text{ km/s}$ . The zero channel corresponds to  $v_{\text{LSR}}=1137 \text{ km s}^{-1}$  of NGC 1068.

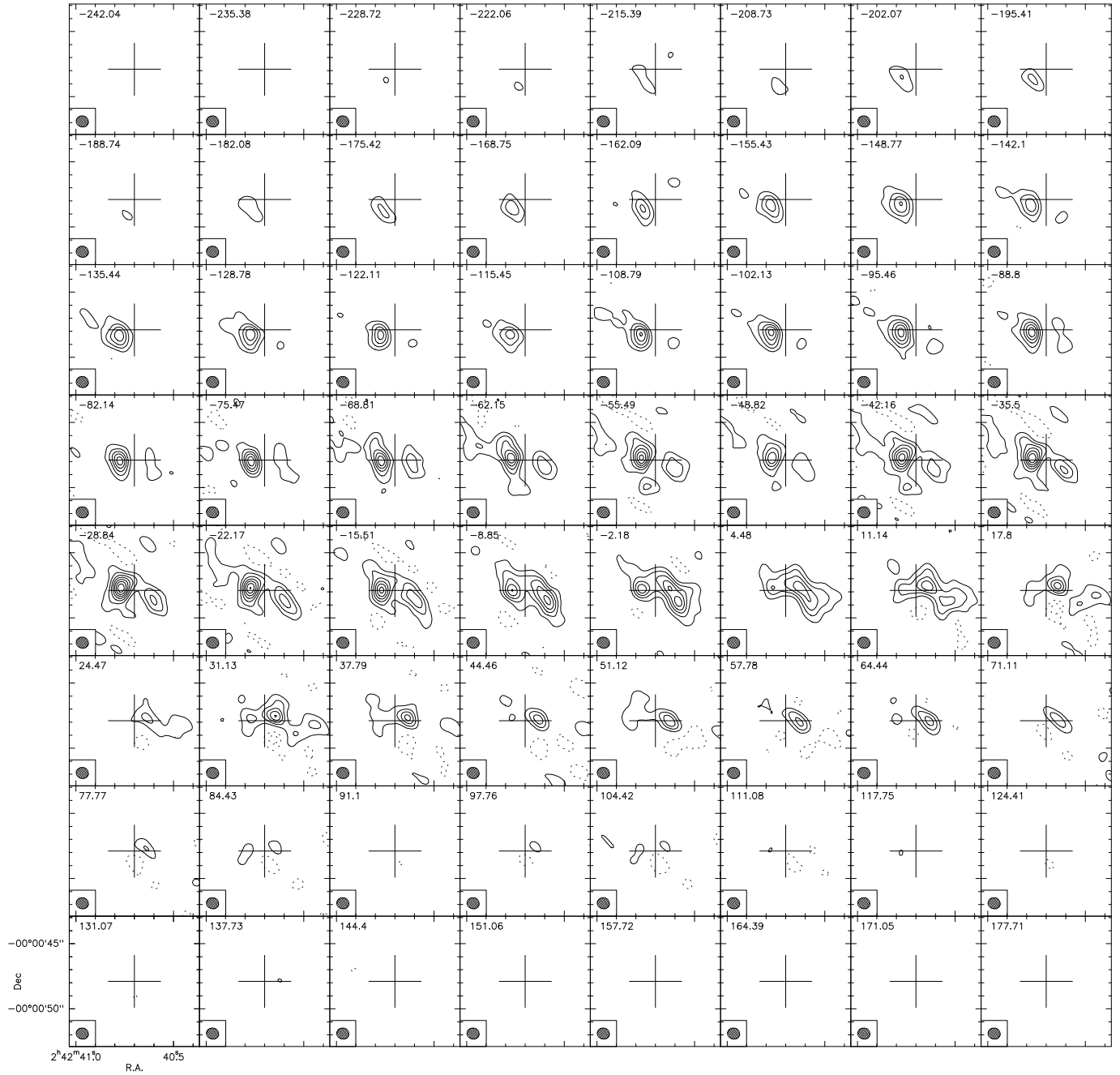


FIG. 8.— Channel maps of the  $^{12}\text{CO}(J=3-2)$  emission in NGC 1068. We use a spectral resolution of  $\sim 7 \text{ km s}^{-1}$  and the original spatial resolution from the observations. Contour spacing is in steps of  $5\sigma=400 \text{ mJy beam}^{-1}$ . The zero channel corresponds to  $v_{\text{LSR}}=1137 \text{ km s}^{-1}$  of NGC 1068.

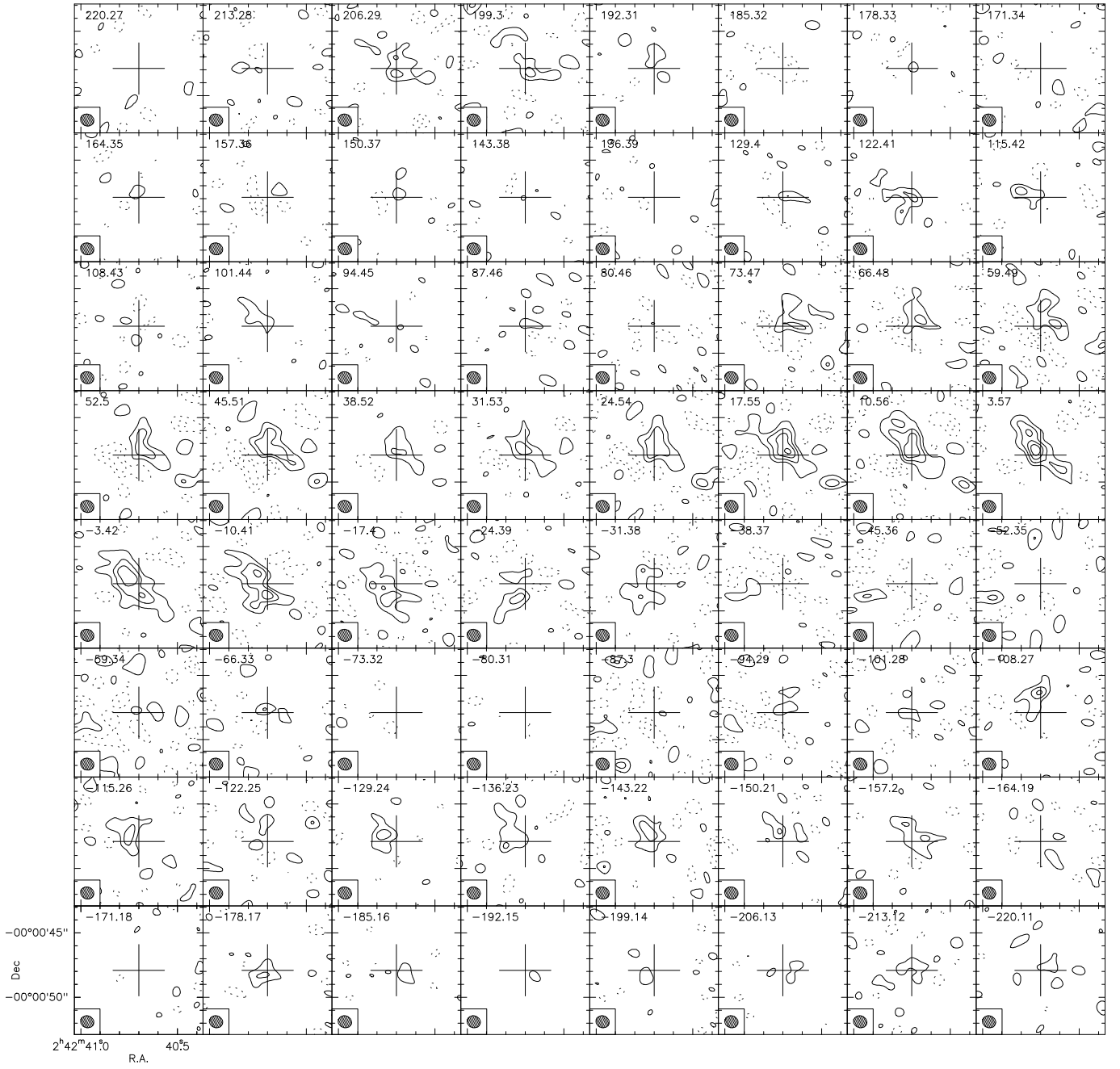


FIG. 9.— Channel maps of the  $^{13}\text{CO}(J=2-1)$  emission in NGC 1068. We use spectral resolution of  $\sim 7 \text{ km s}^{-1}$ . Contour spacing is in steps of  $2\sigma=11 \text{ mJy beam}^{-1}$ . The zero channel corresponds to  $v_{\text{LSR}}=1137 \text{ km s}^{-1}$  of NGC 1068.

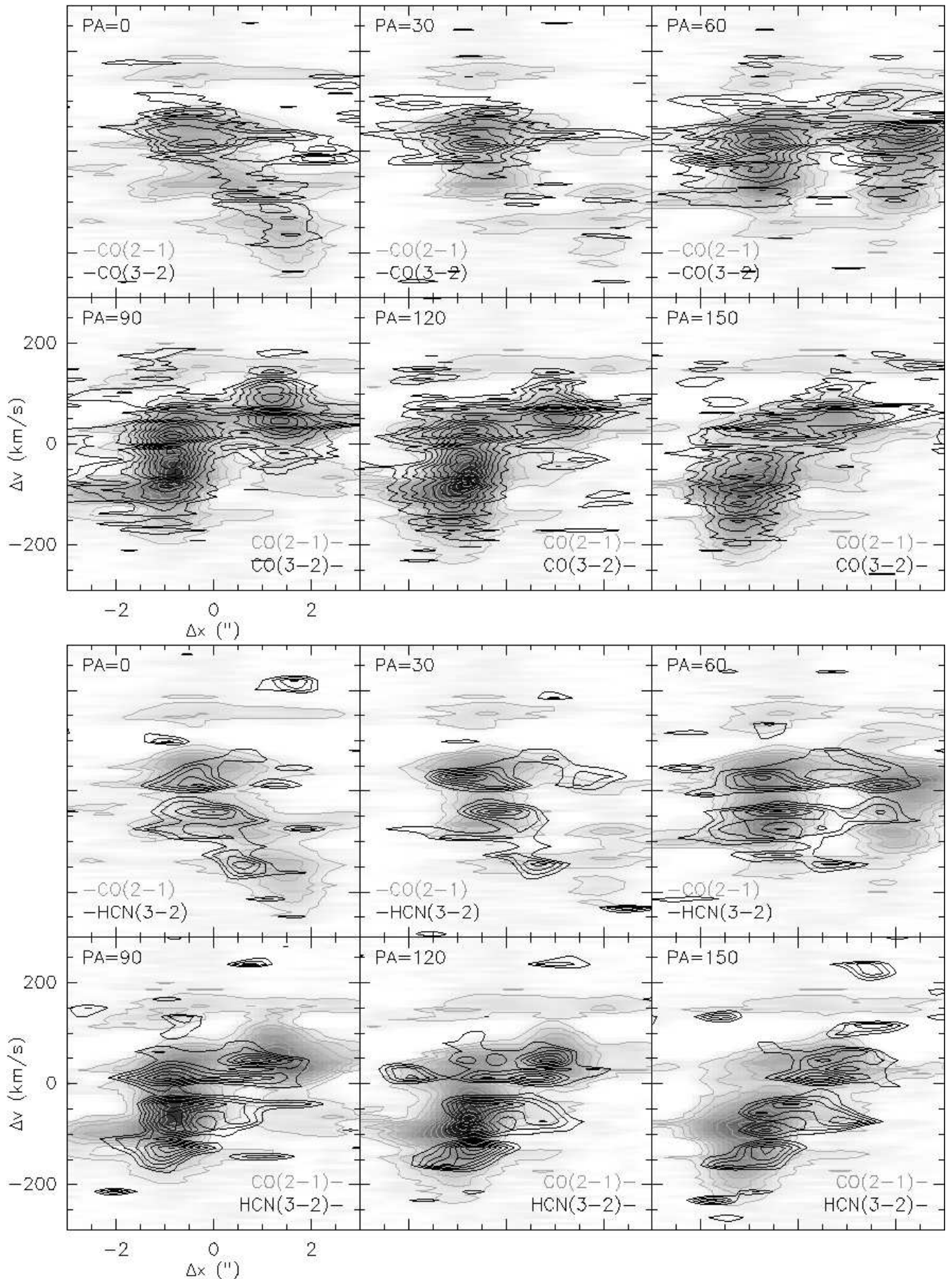


FIG. 10.— Position-velocity diagram of NGC 1068 for the  $^{12}\text{CO}(J=2-1)$  (grey scale),  $^{12}\text{CO}(J=3-2)$  (black contours, top figure) and HCN( $J=3-2$ ) (black contours; bottom figure) emission.

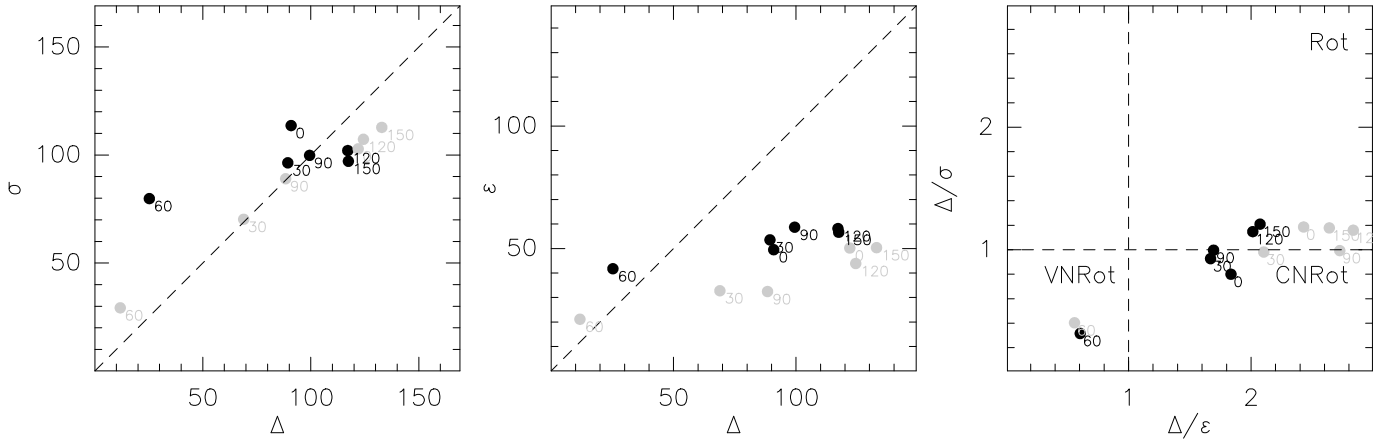


FIG. 11.— Parametrisation of the kinematics in the CND of NGC 1068 for the  $^{12}\text{CO}(J=2-1)$  emission (filled black data points) taken along the slits at different position angles (at 0, 30, 60, 90, 120, and  $150^\circ$ ).  $\sigma$  is the average line-of-sight velocity dispersion,  $\epsilon$  the rms variation of the velocity from point to point and  $\Delta$  the rotational velocity along each slit (see text in Section 5.2 for a more detailed description). VNRot = violent non-rotators, CNRot = calm non-rotators and Rot = rotators. The filled grey data points were determined from the model discussed in Section 5.2.

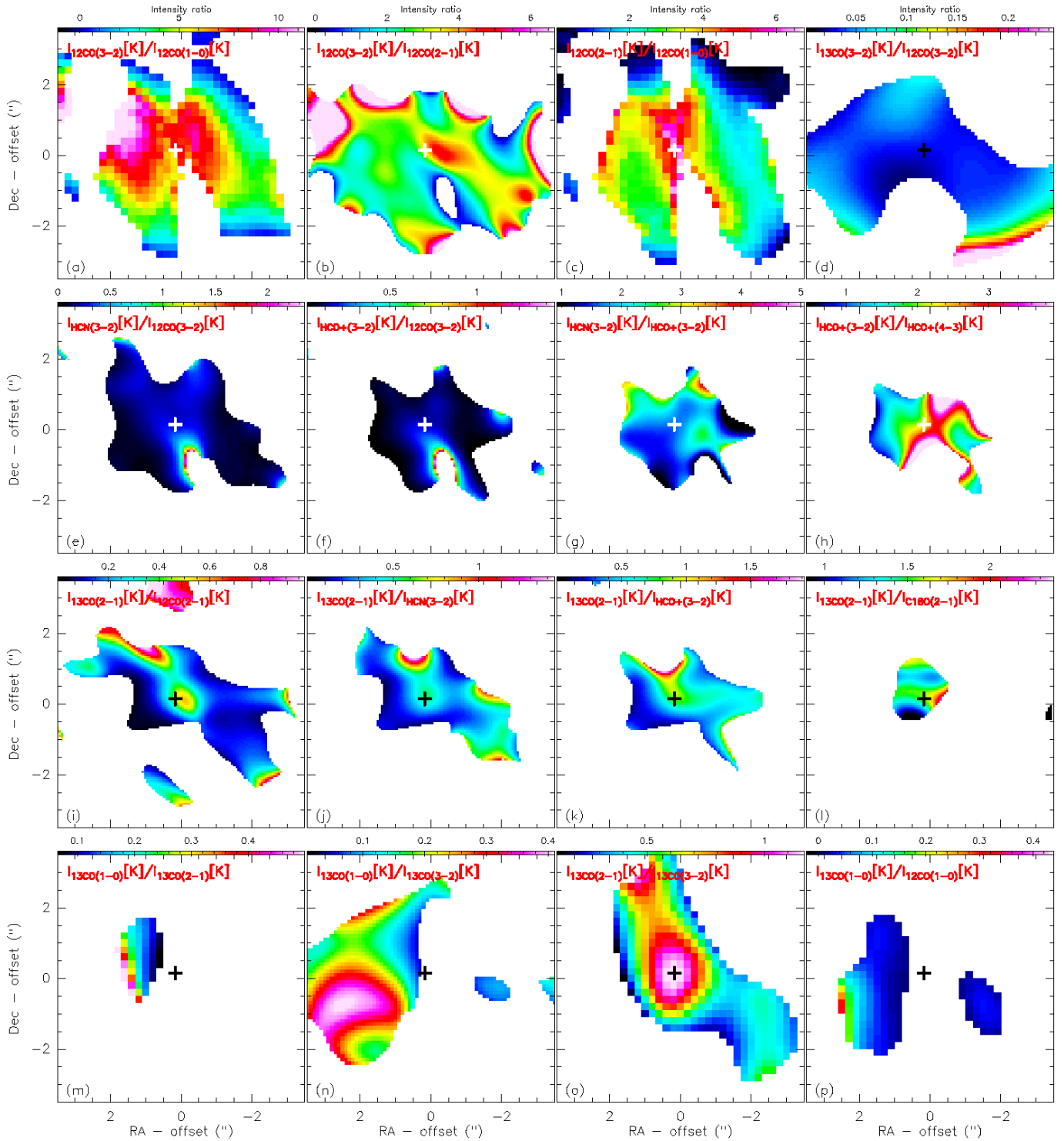


FIG. 12.— Velocity integrated molecular line intensity ratios for NGC 1068 above a  $\geq 1\sigma$  threshold. The white cross marks the position of the mm continuum emission that is associated with the AGN. The different line ratios are: a)  $^{12}\text{CO}(J=3-2)$ -to- $^{12}\text{CO}(J=1-0)$ ; b)  $^{12}\text{CO}(J=3-2)$ -to- $^{12}\text{CO}(J=2-1)$ , c)  $^{12}\text{CO}(J=2-1)$ -to- $^{12}\text{CO}(J=1-0)$ , d)  $^{12}\text{CO}(J=3-2)$ -to- $^{13}\text{CO}(J=3-2)$ , e)  $\text{HCN}(J=3-2)$ -to- $^{12}\text{CO}(J=3-2)$ , f)  $\text{HCO}^+(J=3-2)$ -to- $^{12}\text{CO}(J=3-2)$ , g)  $\text{HCN}(J=3-2)$ -to- $\text{HCO}^+(J=3-2)$ , h)  $\text{HCO}^+(J=3-2)$ -to- $\text{HCO}^+(J=4-3)$ , i)  $^{13}\text{CO}(J=2-1)$ -to- $^{12}\text{CO}(J=2-1)$ , j)  $^{13}\text{CO}(J=2-1)$ -to- $\text{HCN}(J=3-2)$ , k)  $^{13}\text{CO}(J=2-1)$ -to- $\text{HCO}^+(J=3-2)$ , l)  $^{13}\text{CO}(J=2-1)$ -to- $\text{C}^{18}\text{O}(J=2-1)$ , m)  $^{13}\text{CO}(J=1-0)$ -to- $^{13}\text{CO}(J=2-1)$ , n)  $^{13}\text{CO}(J=1-0)$ -to- $^{13}\text{CO}(J=3-2)$ , o)  $^{13}\text{CO}(J=2-1)$ -to- $^{13}\text{CO}(J=3-2)$ , p)  $^{13}\text{CO}(J=1-0)$ -to- $^{12}\text{CO}(J=1-0)$

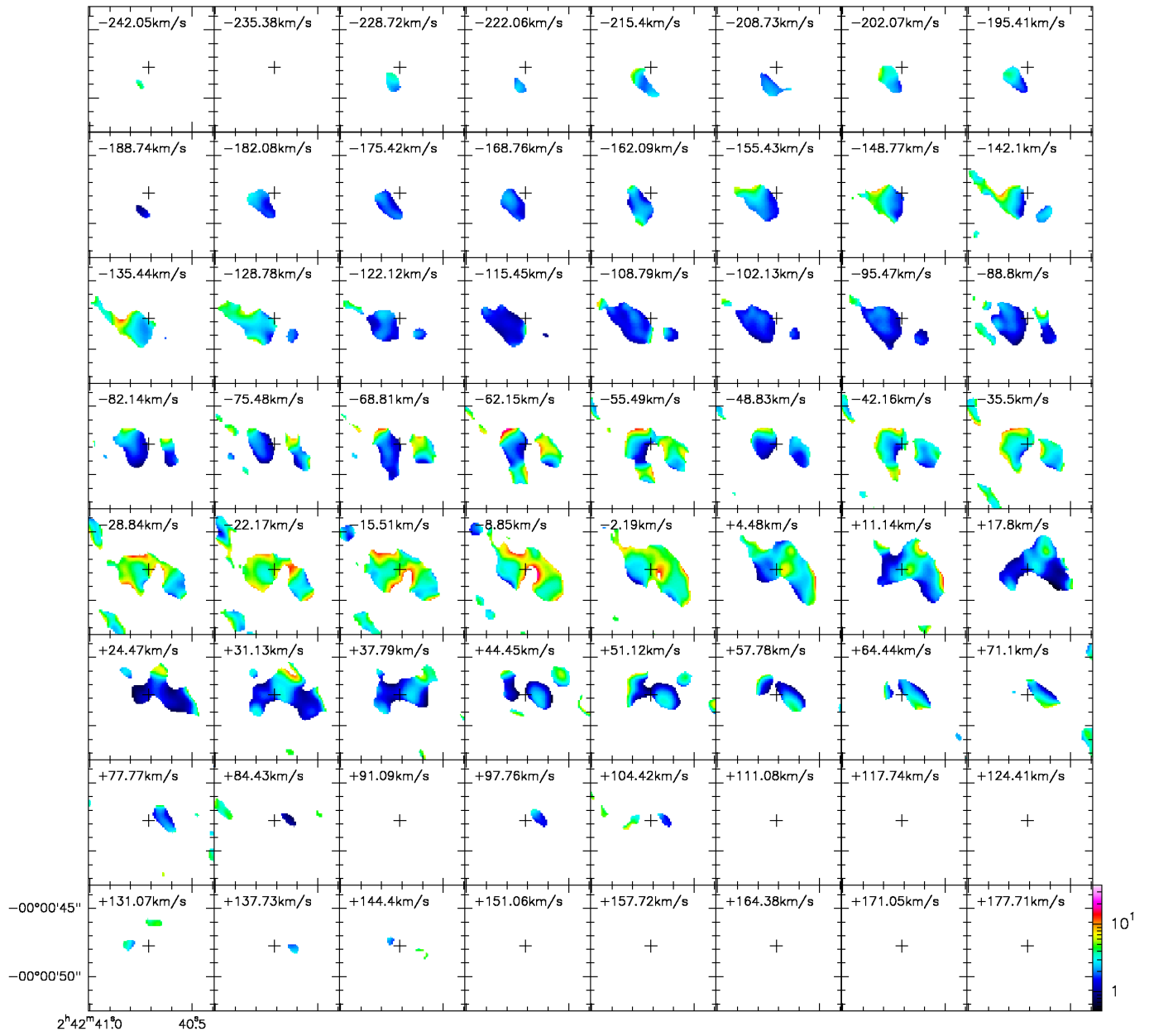


FIG. 13.—  $^{12}\text{CO}(J=3-2)$ -to- $^{12}\text{CO}(J=2-1)$  line ratio above a  $4\sigma$ -threshold for each line.

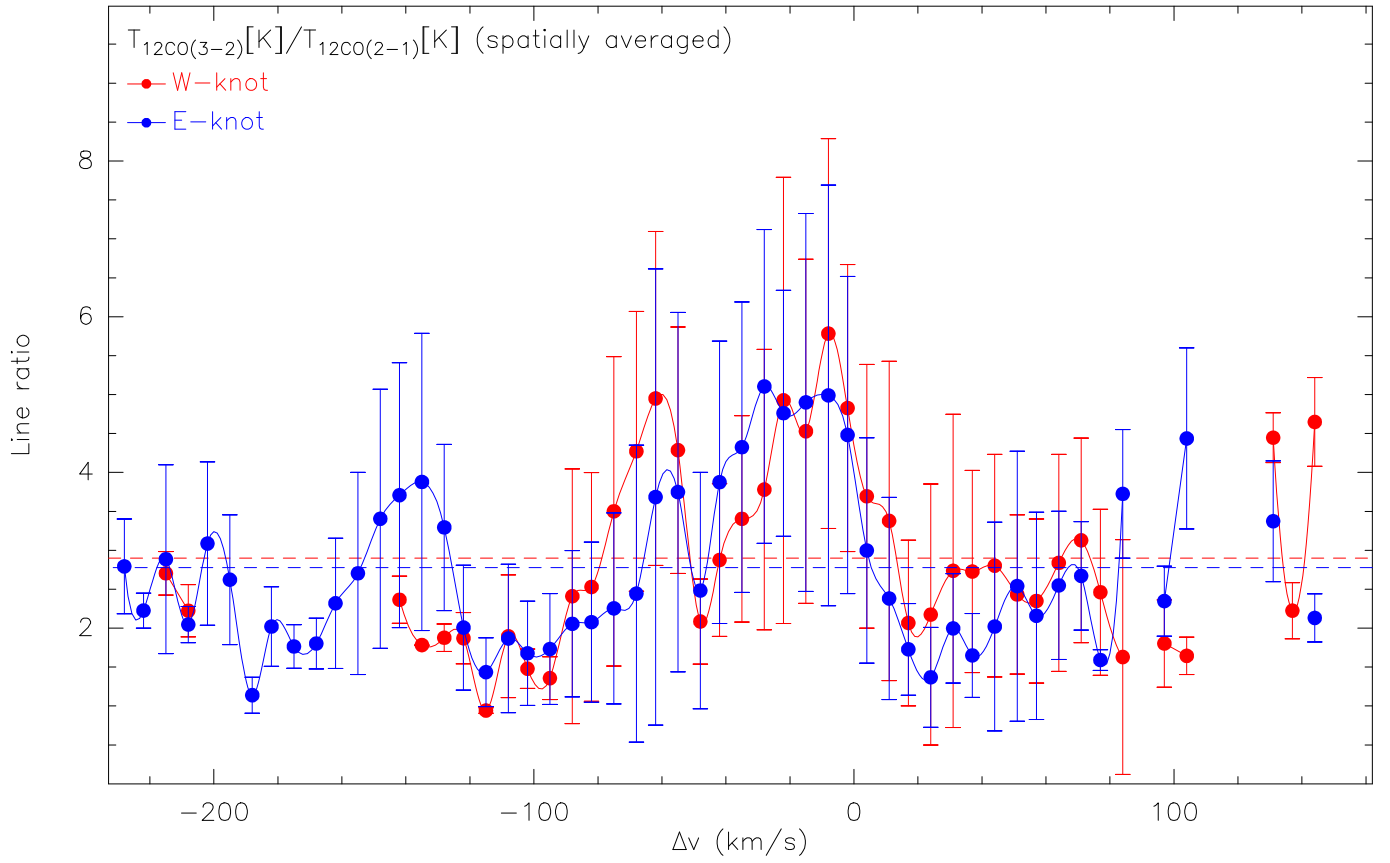


FIG. 14.— Spatially averaged line ratio for the eastern and western knot as function of velocity, derived from Fig. 13. The error bars denote the variance of each averaged value, which does not exceed 50% in most cases. The missing values for velocities  $-120$  and  $-200$   $\text{km s}^{-1}$  and  $+100$  to  $+140$   $\text{km s}^{-1}$  are due to the lack of emission in the respective knot. The dashed lines represent the median of the line ratios for the two knots.

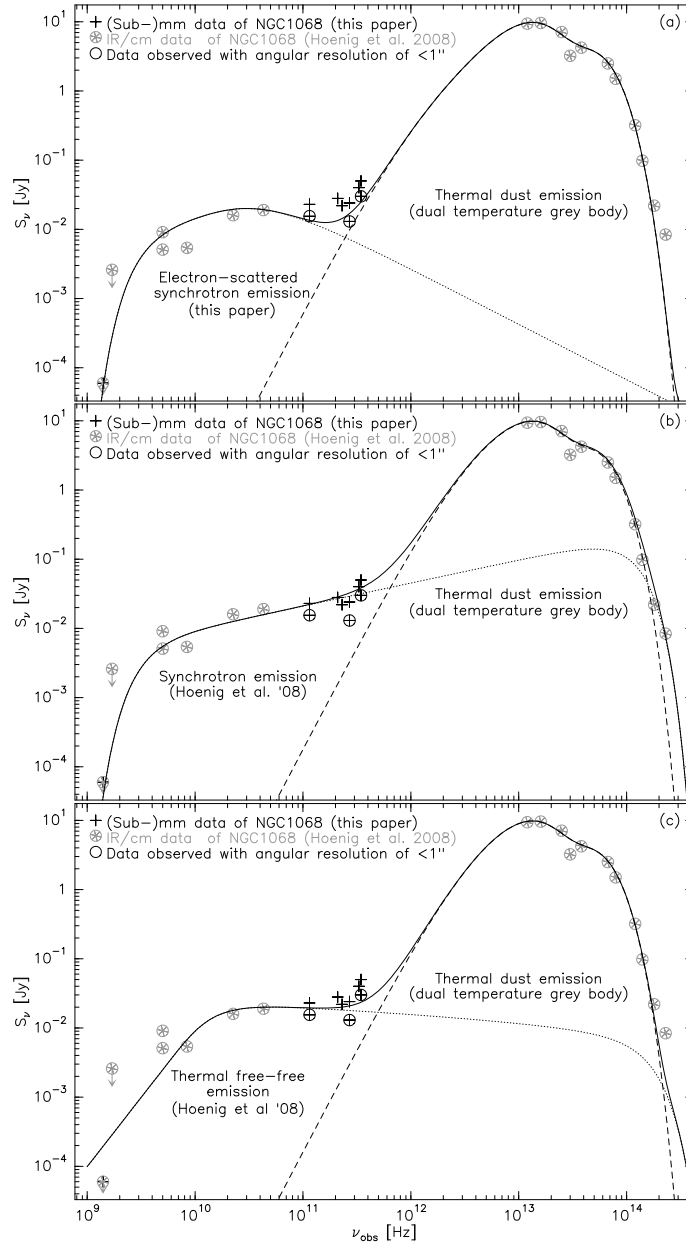


FIG. 15.— Spectral energy distribution of the continuum emission in NGC 1068, based on data from this paper, Krips et al. (2006) (*black crosses*), and Hönig et al. (2008) (*grey crosses*). The dotted line represents the model for the radio continuum emission (either electron scattered synchrotron emission (a), synchrotron emission (b), and free-free absorption (c)), the dashed line represents the model for the IR data (a two-temperature grey body a-c), and the solid line represents the composite of both (a-c). The data observed at an angular resolution below  $1''$  are additionally marked with a circle.

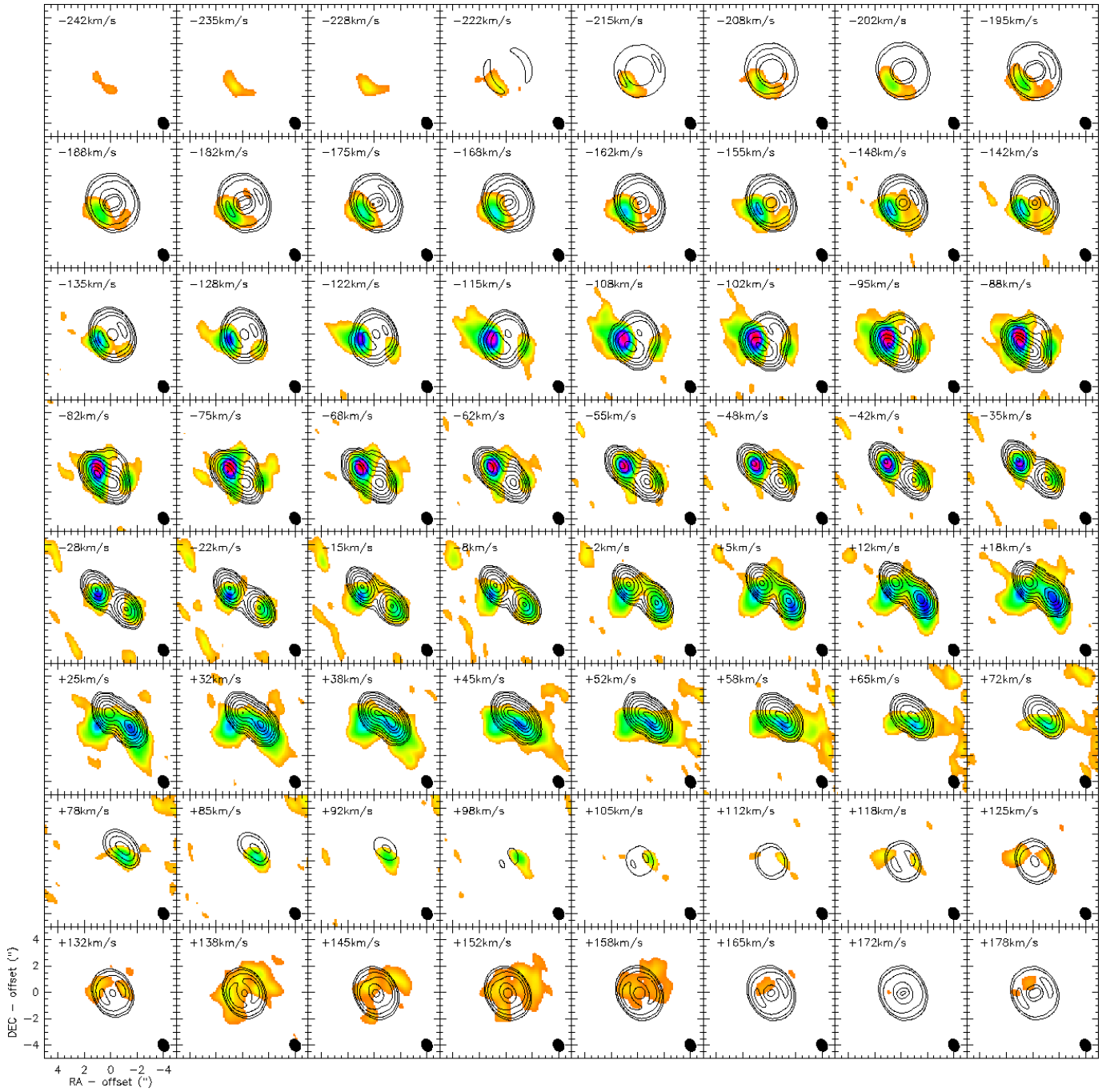


FIG. 16.— Velocity channel maps of the CO model compared to the  $^{12}\text{CO}(2-1)$  emission.

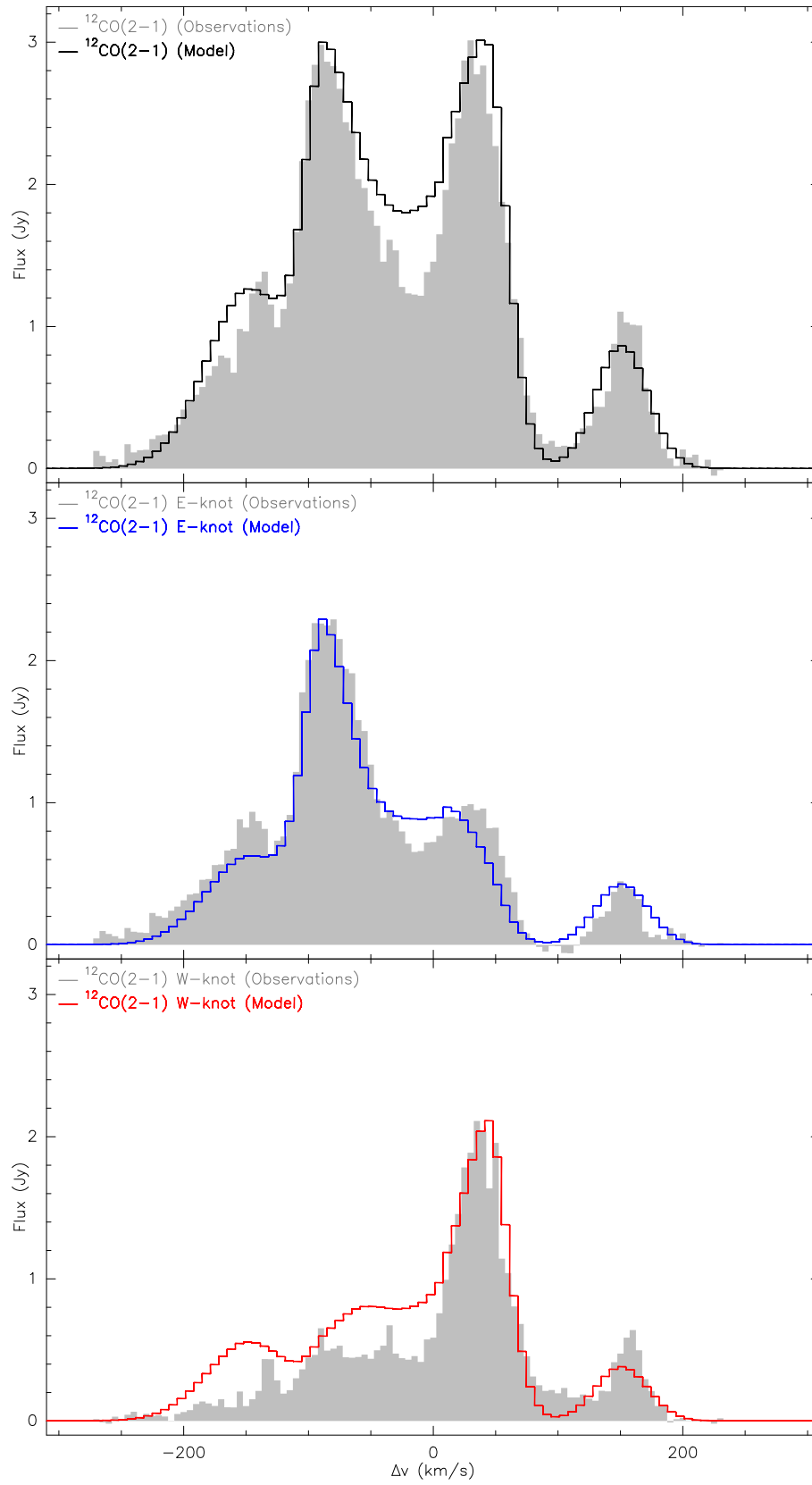


FIG. 17.— Spectrum of the CO model compared to the  $^{12}\text{CO}(2-1)$  emission.

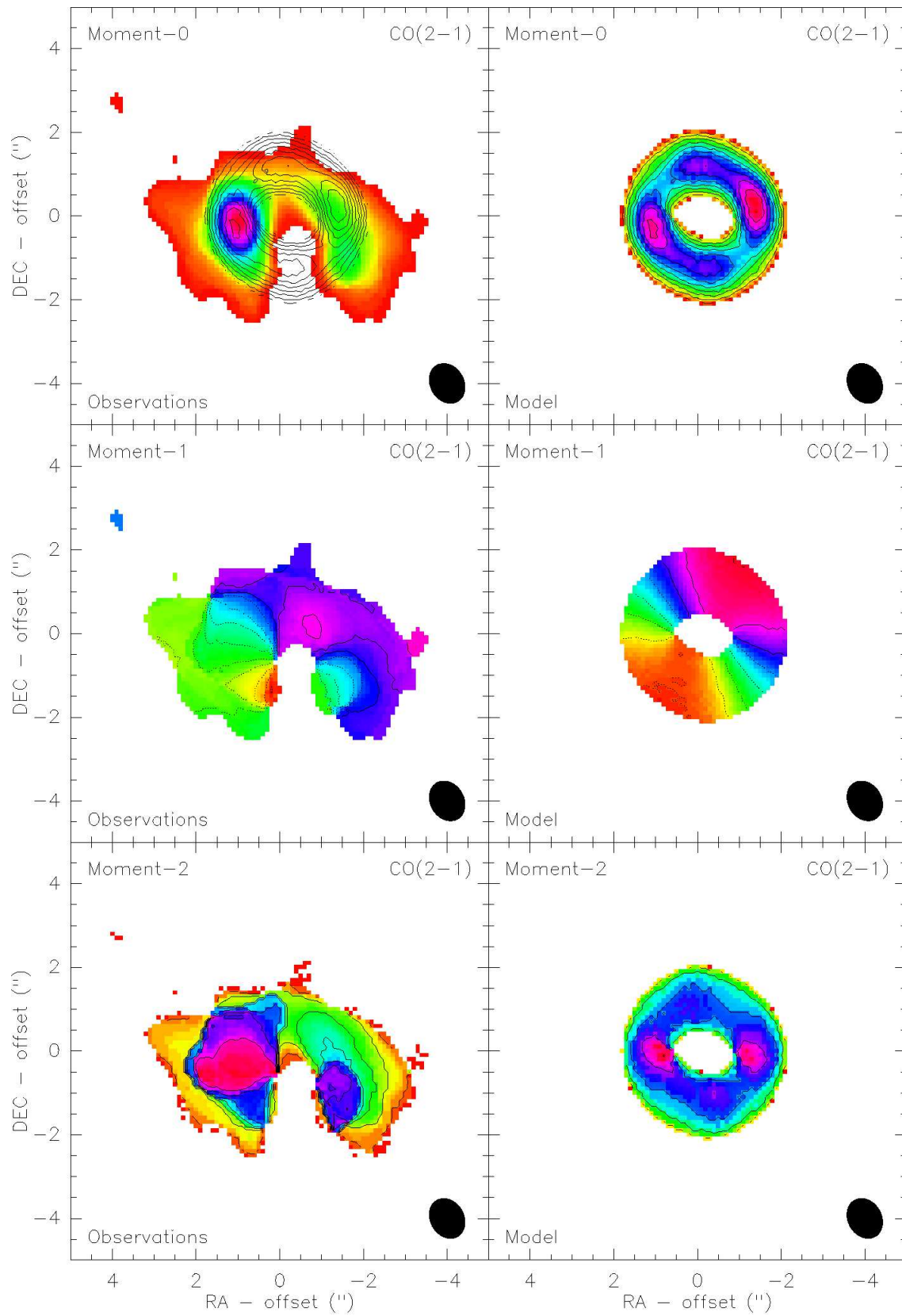


FIG. 18.— Moment maps of the CO model compared to the  $^{12}\text{CO}(2-1)$  emission. The velocities are plotted in steps of  $20\text{km s}^{-1}$  for the Moment-1 and Moment-2 maps.

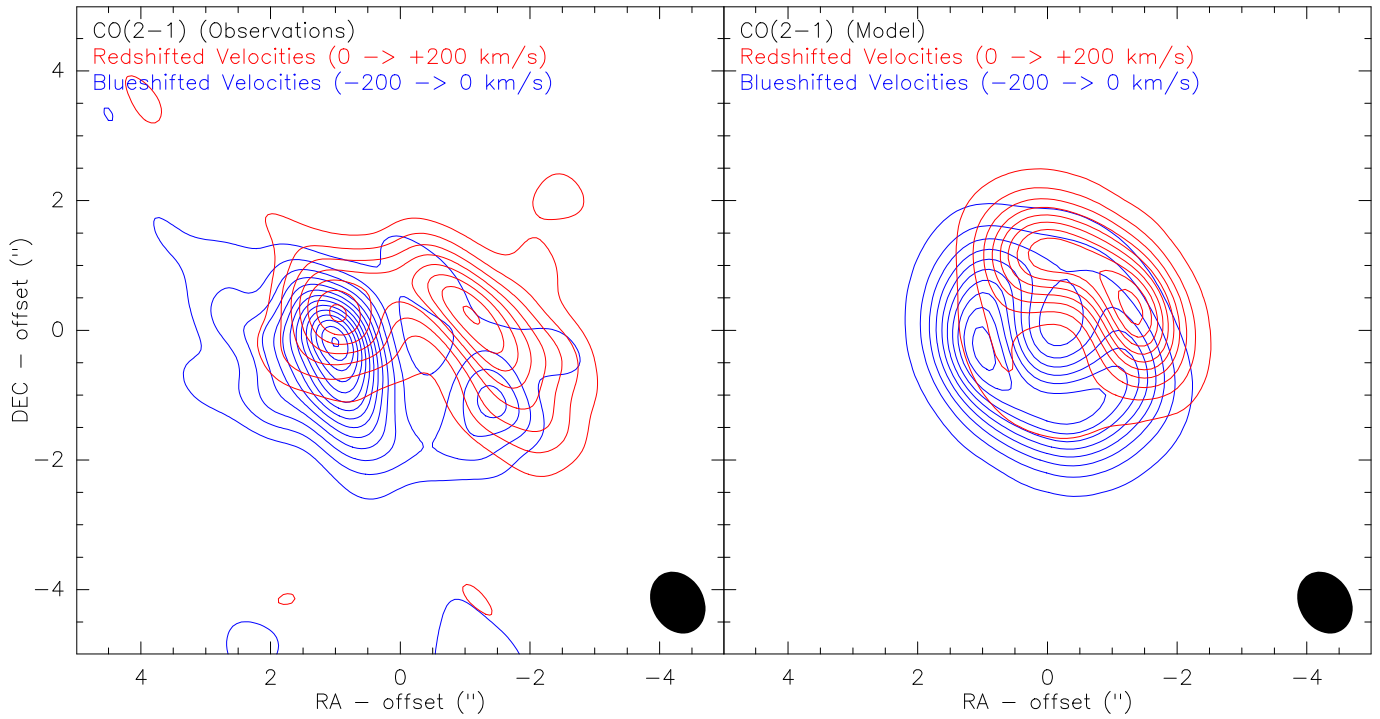


FIG. 19.— Blue- and Redshifted emission of the CO model compared to the  $^{12}\text{CO}(2-1)$  emission.

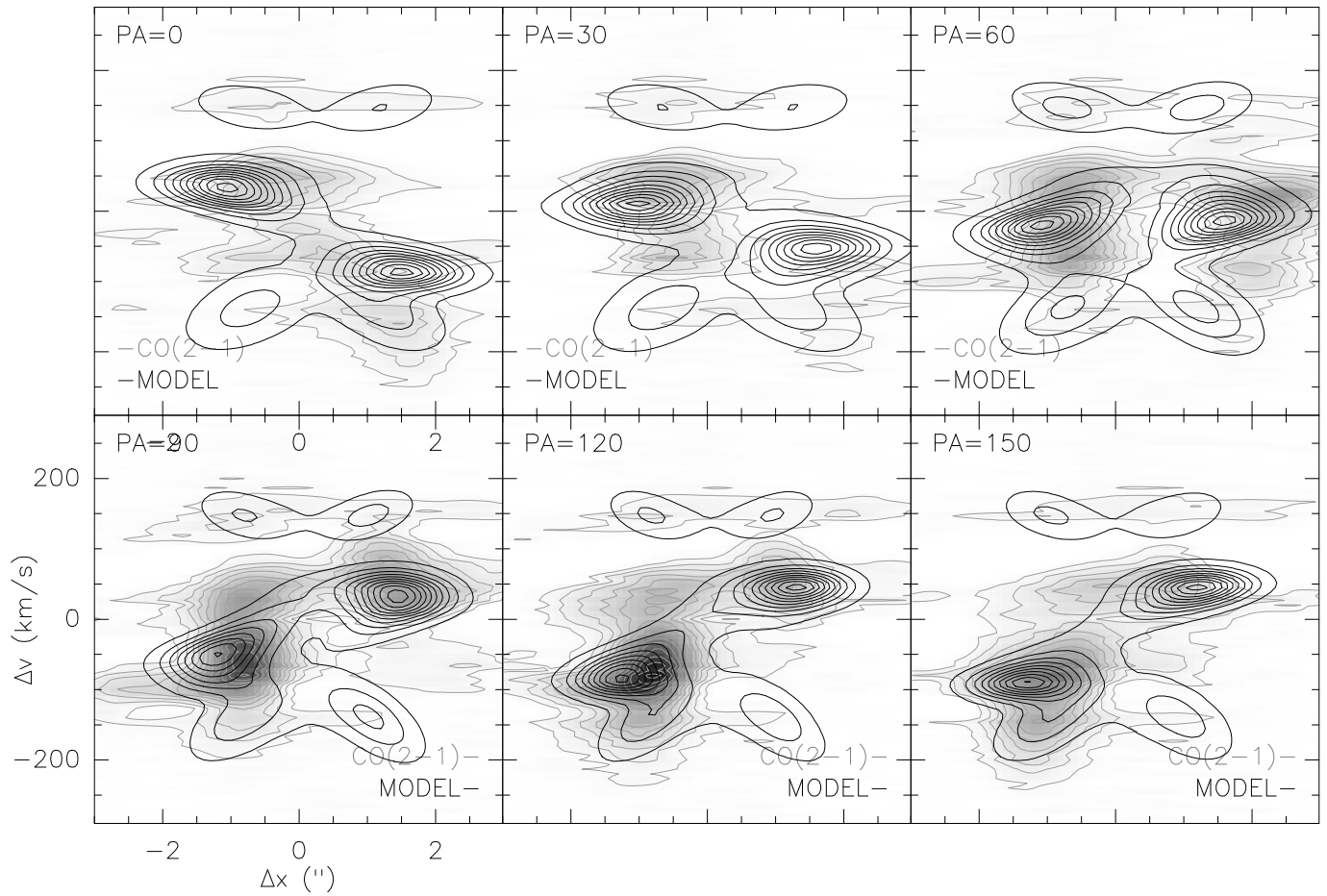


FIG. 20.— Position-velocity diagram of the CO model compared to the  $^{12}\text{CO}(2-1)$  emission.

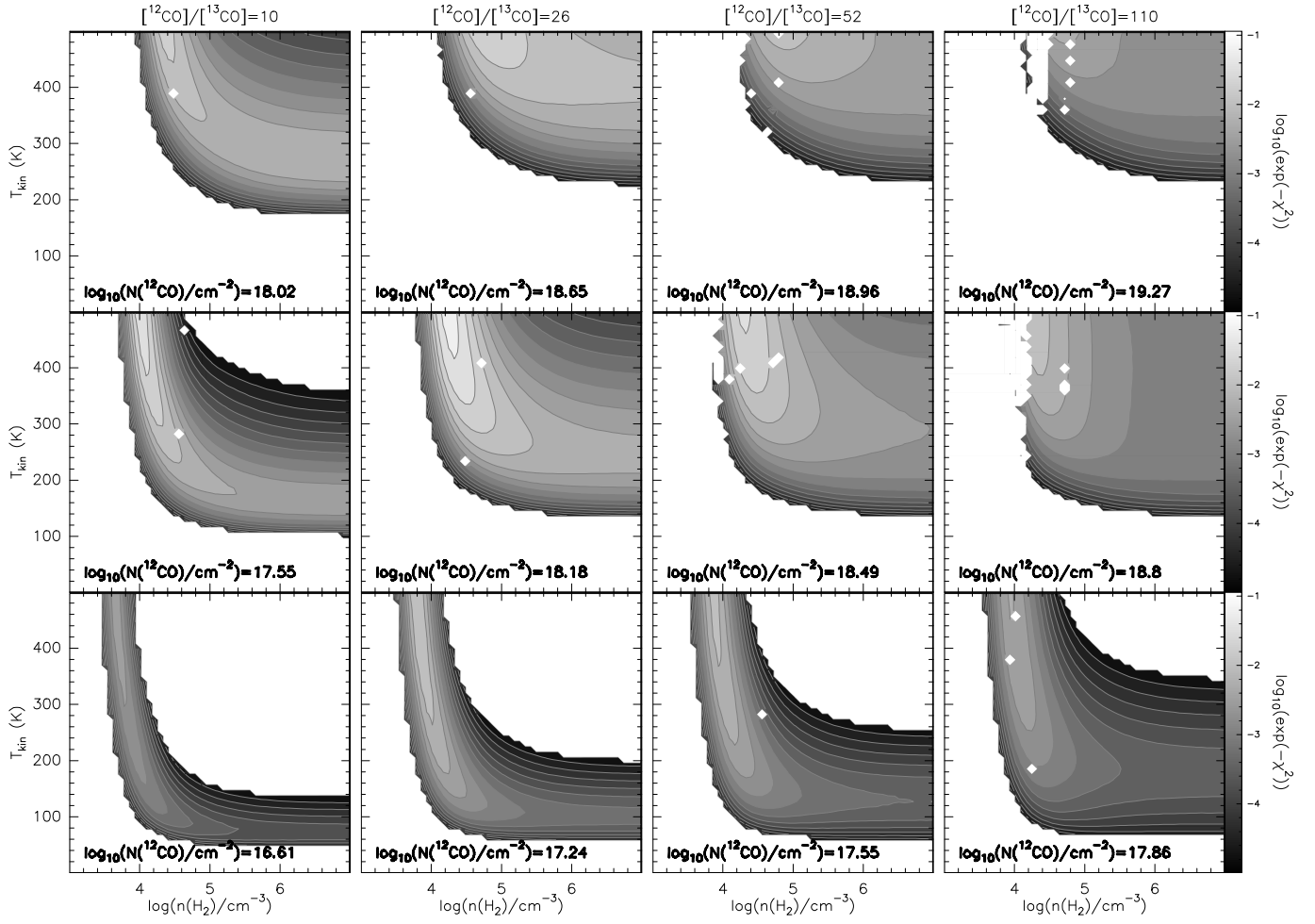


FIG. 21.—  $\chi^2$ -fit results obtained from the RADEX simulations of the excitation conditions of the molecular gas. Shown are four different  $^{12}\text{CO}/^{13}\text{CO}$  abundance ratios ( $=10, 26, 52, 110$ ) for three different  $^{12}\text{CO}$  column densities respectively. The middle panel shows the best  $\chi^2$ -fit found for each abundance ratio.

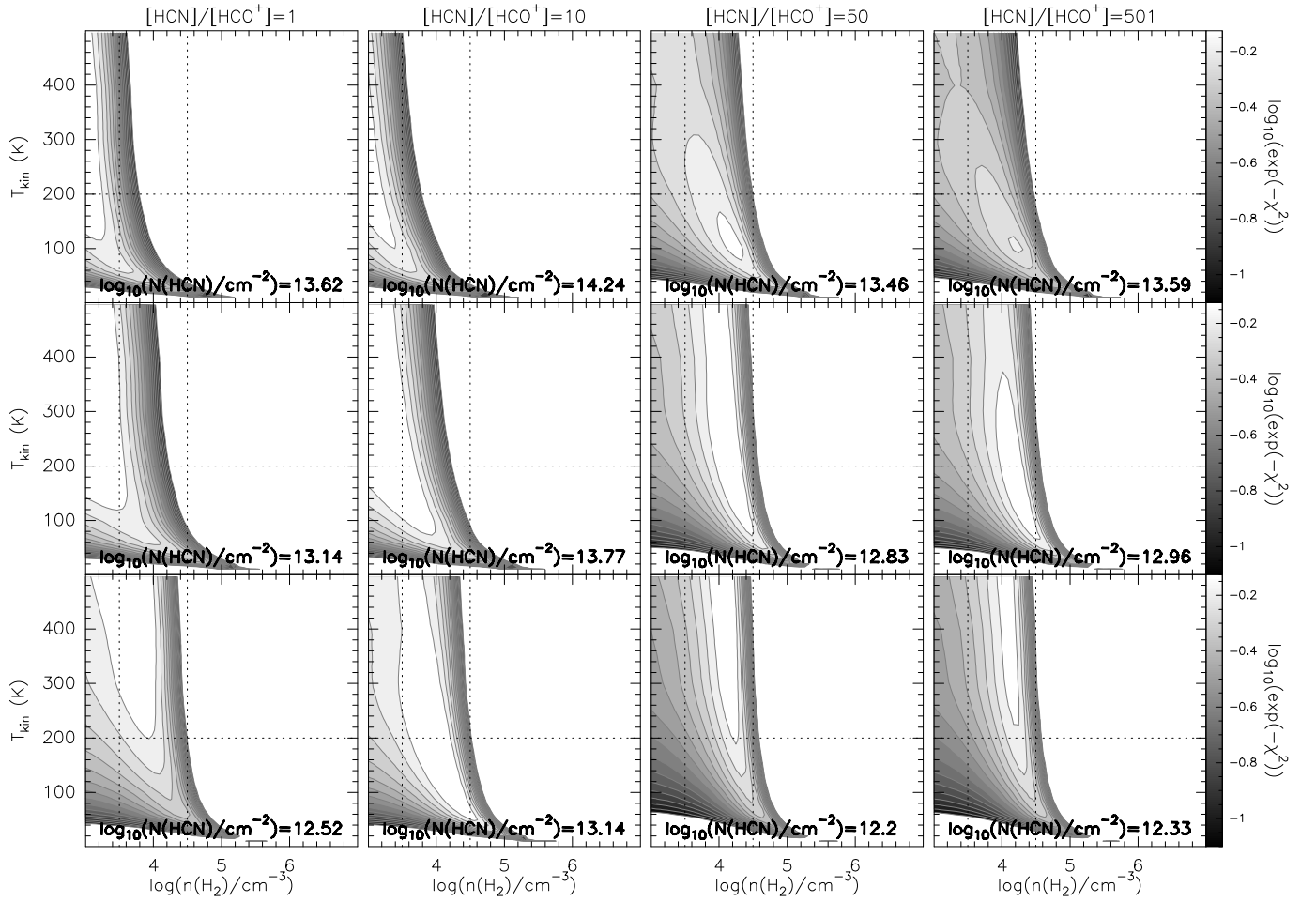


FIG. 22.—  $\chi^2$ -fit results obtained from the RADEX simulations of the excitation conditions of the molecular gas. Shown are four different  $[\text{HCN}]/[\text{HCO}^+]$  abundance ratios around the standard galactic value of  $[\text{HCN}]/[\text{HCO}^+] \simeq 10$  for three different HCN column densities respectively. The middle panel shows the best  $\chi^2$ -fit found for each abundance ratio.